# Characterization of high-Q ultralight membranes towards novel optomechanical designs

MSc Thesis in Physics, 2021-2022

*Zihua Wang*

Supervisors:

*Prof. Eugene Simon Polzik and Dr. Georg Enzian*

University of Copenhagen

| | | |
|---|---|---|
| Faculty: | Faculty of Science | |
| Institute: | The Niels Bohr Institute | |
| Author: | Zihua Wang | KU-ID: tfk141 |
| Email: | tfk141@alumni.ku.dk or zihuadanielwang@hotmail.com | |
| Title: | Characterization of high-Q ultralight membranes towards novel optomechanical designs | |
| Supervisor: | Prof. Eugene Simon Polzik | polzik@nbi.ku.dk |
| Co-Supervisor: | Dr. Georg Enzian | georg.enzian@nbi.ku.dk |
| Handed in: | May, 2022 | |


**Abstract**

Thin silicon nitride membranes with a photonic crystal and high-contrast gratings are promising devices for cavity optomechanics, that could potentially lead to new designs. In the thesis we present analysis on a such highly reflective silicon nitride membrane featuring high mechanical quality factor and discuss its applicability for cavity optomechanics. The membrane, combining photonic and phononic crystal patterns, reaches reflectivities up to 0.9989 and a mechanical quality factor of $2.4 \times 10^7$ at room temperature in vacuum.

With the membrane forming one mirror of an optical cavity, we observe the optomechanically induced optical bistability, birefriengence as well as a clover-leaf-shaped transmitted beam shape. We support an understanding of its emergence by implementing a scalar Fox-Li algorithm to solve for the fundamental mode of the cavity and feeding it with an incident-angle-dependent reflectivity of the photonic crystal reflector obtained from COMSOL multiphysics simulation.

The membranes are suitable for reaching high optomechanical cooperativities desirable for optomechanical sensing or squeezing applications.

# Contents

# 1 Introduction

Cavity optomechanics has been studied based on the understanding that light, or photons have momentum. It has been found that light can emit radiation and gradient forces on particles[1], but normally this phenomenon is very weak. However, within a cavity the power can be increased significantly and build up to a level that can push macroscopic items. Membranes, for instance, are one of the most commonly used macroscopic item that can interact with photons. The phononic bandgap simulation and designs were done in Niels Bohr Institute back in 2017. [2]

Reaching high optomechanical cooperativity is desirable for many optomechanical schemes and applications. It quantifies the coherent interaction between optical and mechanical degrees of freedom of a system of interest in relation to their respective dissipation rates. In many cases cooperativity is a parameter representing the limit of device performance in sensing or cooling performance in optomechanical quantum state engineering schemes. Thus finding ways to increase it is desirable both for practical applications as well as fundamental studies in cavity optomechanics.

Reaching high optomechanical cooperativity in cavity optomechanics entails confining light and mechanical vibration into a small region of space, while managing the dissipation. Coupling can arise due to the radiation pressure exerted by the light onto mechanically compliant material boundaries or due to electrostriction in the bulk material, and both mechanisms have been exploited to reach high optomechanical cooperativities [3].

In recent years, thin mechanically compliant membranes suspended inside an optical cavity (membrane-in-the-middle MIM [4]) have attracted growing interest. Here the mechanical and optical resonators can be designed relatively independently compared with other optomechanical platforms and optimised in order to mitigate losses. In particular, silicon nitride membranes have been successfully used in a plethora of optomechanical experiments.

Building upon the advantages of the MIM-platform and minimising the mechanical dissipation of the silicon nitride membranes' modes of oscillation to reach Q-f-products of $> 10^{17}$ [2] have recently enabled several demonstrations of quantum-limited operation and exploitation of quantum effects in optomechanics [5, 6, 7].

As is well-known [4], the linear dispersive optomechanical coupling rate in the MIM system increases with the reflectivity, as well as possesses a steepening and shallowing slope of the dispersion when the membrane is moved away from the middle of the cavity. Aside from reaching high mechanical quality in the MIM system, it is thus also desirable to have a highly reflecting membrane in order to maximize the optomechanical interaction.

While small coupling rates per photon can in principle be compensated by increasing the intracavity power in linearized optomechanics, undesired heating still represents a significant challenge in quantum optomechanics [**?** ] and avoiding high pump power levels to reach certain parameters might prove a crucial ingredient to further the quantum prospects of optomechanical schemes. In previous work by Chen et al. [8] highly reflecting photonic crystal slabs of stressed silicon nitride were demonstrated.

Here we present experiments with high mechanical quality silicon nitride membranes which, additionally to their phononic patterning, feature a highly reflective photonic crystal structure on their central defect.

In section 2 we provided some knowledge and obtained some results on cavity optics that will be heavily used in the thesis. In section 3 we gave an introduction to early membrane overall inspections on their photonic and phononic structures, as well as some early tests and comments on their optical and mechanical qualities. In section 4 we demonstrated the setups and measurement techniques used in the experiment as well as the final results that we obtained. In section 5, we discussed and investigated some of the side effects we observed in our cavity experiment, and highlighted the "clover shape" beam that hasn't been observed before by other articles. In section 6, some of the methods that we tried and developed for result analysis were discussed, and their advantages and disadvantages were compared. Finally, in section 7, we combined COMSOL and Python simulations to provide a promising explanation for the origin of the newly found "clover shape" beam.

# 2 Theoretical Background

## 2.1 Fabry-Perot cavity theory

Our approach to measure the cavity quality included the assembly of a Fabry-Perot cavity with a mirror and a membrane shown in Figure 1.

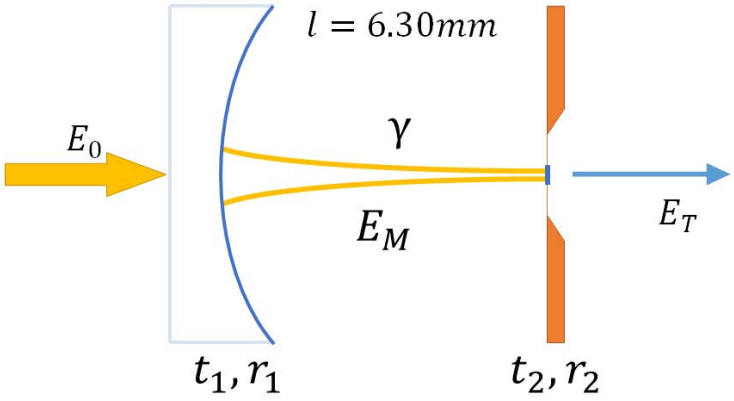


Figure 1: Cavity used for membrane characterization. The front mirror used on the left is a 500 ppm or 1000 ppm concave mirror, and the PhC membrane on the right works as a highly reflective back mirror. $\gamma$ is the round trip loss of the cavity, $t_1$ and $r_1$ represent the transmission and reflection coefficient of the input mirror, and $t_2$ and $r_2$ represent the transmission and reflection coefficient of the output mirror(photonic crystal membrane). l is the cavity length whose value will be acquired later in 4.3.2.

A simple theory includes the transmission and reflection relations with the round trip loss $\gamma$, transmission and reflection coefficients.

Let us first consider the case shown in Figure 1 above, in which our light is being reflected back and forth between the two low-transmission mirrors. Here, we use the following approximations:

$$r_1 \approx r_2 \approx 1 \tag{1}$$

### 2.1.1 Transmission

We can start with the simple case of cavity transmission calculation shown in Figure 1.

The amplitude of light entering the cavity is:

$$E_1 = E_0 t_1 \tag{2}$$

Where $E_0$ is the input electric field strength. When our cavity is on resonance, we know that the light inside the cavity forms a standing wave, thus we should add up to the intracavity electric field strength $E_M$ in order to include all the amplitudes of light bouncing back and forth inside our cavity. Through each round trip there is a power attenuation of $1-\gamma$, which corresponds to amplitude loss of $(1-\gamma)^{\frac{1}{2}}$.Thus, together with Equation 2 we can conclude that the amplitude inside the cavity is:

$$\begin{aligned} E_M &= E_1 \times [1 + (1-\gamma)^{\frac{1}{2}} + (1-\gamma)^1 + (1-\gamma)^{\frac{3}{2}} + ...] \\ &\approx E_1 \times \frac{2}{\gamma} \\ &= \frac{2E_0 t_1}{\gamma} \end{aligned} \tag{3}$$

Since both sides can still transmit a small proportion of light, we know that there will be a leakage of light from both mirrors, and the leakage to the right hand side $E_T$ will be the transmission amplitude. After we compare that value with $E_0$ we can conclude:

$$\begin{aligned} T = \frac{E_T^2}{E_0^2} &= \frac{E_M^2 \times t_2^2}{E_0^2} \\ &= \frac{4t_1^2 t_2^2}{\gamma^2} \end{aligned} \tag{4}$$

This is the theoretical transmission we should expect for our cavity, that we will come in handy later in section 6 for result analysis.

### 2.1.2 Reflection

As for the reflection side of the cavity, we should first consider the model shown in Figure 2.

We can see that in order to calculate the reflection amplitude $E_R$, we should consider two contributions to it: reflection amplitude $E_{0R}$ from the concave mirror and the leakage from the cavity $E_{MR}$. Please note that here $E_{M2}$ is slightly different from $E_M$ we calculated from Equation 3, due to a different propagation direction of waves. But we can calculate them in the similar way as we used in subsubsection 2.1.1 and Equation 1 to simplify the equations:

$$\begin{aligned} E_{0R} &= E_0 \times r_1 \\ &\approx E_0 \end{aligned} \tag{5}$$

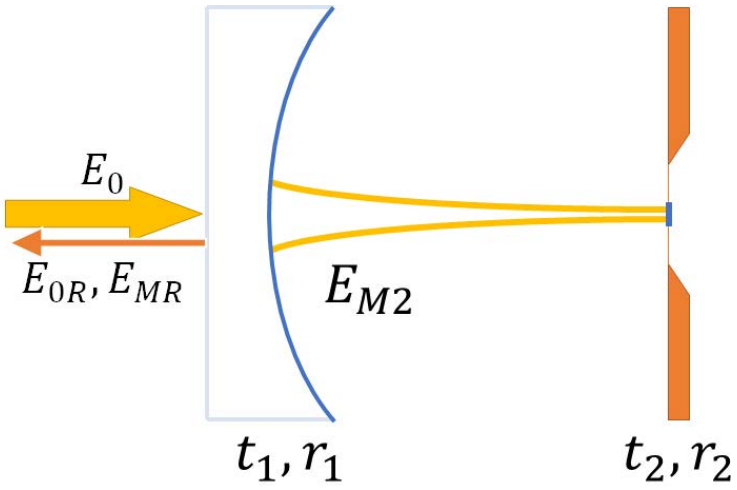


Figure 2: Reflection amplitude $E_0R$ from the concave mirror and the leakage from the cavity $E_MR$ contribute together for the total reflection amplitude $E_R$.

$$\begin{aligned} E_{MR} = E_{M2} \times t_1 &= E_1 \times r_2 \times [1 + (1-\gamma)^{\frac{1}{2}} + (1-\gamma)^1 + (1-\gamma)^{\frac{3}{2}} + ...] \times t_1 \\ &\approx E_0 \times t_1^2 \times r_2 \times \frac{2}{\gamma} \\ &\approx \frac{2E_0 t_1^2}{\gamma} \end{aligned} \tag{6}$$

Here, $E_0R$ with $E_MR$ has a phase difference of $\pi$ due to the reflection phase shift from the concave mirror. After we achieve these results, and due to the phase difference between them, we can obtain the steady state reflection amplitude from the resonant cavity by subtraction:

$$E_R = E_{0R} - E_{MR} = E_0 \times (1 - \frac{2t_1^2}{\gamma}) \tag{7}$$

The power reflectivity is then straightforwardly obtained by relating the reflected field to the incoming field $E_0$:

$$\begin{aligned} R &= \frac{E_R^2}{E_0^2} \\ &= (1 - \frac{2t_1^2}{\gamma})^2 \end{aligned} \tag{8}$$

This is the theoretical reflection we should expect from our cavity.

## 2.2 Round trip loss and Finesse

The calculation from our last section requires a very important value: the round trip loss $\gamma$. And our evaluation of round trip loss came from a very important observable quantity: Finesse. Before I introduce Finesse, I need to briefly summarize some other important quantities.

### 2.2.1 Free Spectral Range (FSR)

The free spectral range (FSR) of an optical cavity is the spacing of two nearby resonator modes from the same "mode family" in terms of optical frequency. It is also called axial mode spacing. For an empty(or in vacuum) standing-wave resonator of length L, it can be calculated as:

$$\Delta\nu_{\mathrm{FSR}} = \frac{c}{2l} \tag{9}$$

Here c is the speed of light. This can be intuitively understood as the frequency interval after which the round trip phase has changed by $2\pi$(so it can go back to resonance again).

This quantity can be acquired when we tune our laser wavelength until the second(or $n$th) fundamental resonance peak shows up on our oscilloscope again. Or we can also use a piezo to tune the length of the cavity until we observe the same peak, but this is less convenient than the previous approach, because we need some extra calibrations on the piezo in order to acquire the equivalent frequency changes.

Since we are measuring the difference of wavelength instead of frequency directly, Equation 9 in our case is only for cavity length calculation instead of FSR calculation:

$$l = \frac{c}{2\Delta\nu_{\mathrm{FSR}}} \tag{10}$$

When we use the laser tuning method to measure FSR as we are going to do in 4.3.2, we can acquire wavelength $\lambda$ and the change of wavelength per FSR, we mark it as $\delta\lambda$. We should remember that one FSR changes correspond to $1\lambda$ for each round trip by definition. Thus, we have the frequency- wavelength relation:

$$\begin{aligned} f &= \frac{c}{\lambda} \\ \frac{\delta\lambda}{\lambda} &= \frac{\lambda}{2l} \end{aligned} \tag{11}$$

Finally, from Equation 11 we can get a new expression for FSR:

$$\begin{aligned}\Delta\nu_{\mathrm{FSR}} &= \frac{\lambda}{2l} \times f \\ &= \frac{\delta\lambda}{\lambda} \times f \\ &= \frac{c \times \delta\lambda}{\lambda^2}\end{aligned} \tag{12}$$

### 2.2.2 Cavity linewidth

Full Width at Half Maximum(FWHM) is defined as the difference between the two values of the independent variable at which the dependent variable is equal to half of its maximum value. The value can be better comprehended as shown in Figure 36.

During our experiment, I used Python to fit a Lorentzian shape to our experimental data in order to get the estimated value of FWHM. An EOM in the experiment is used to phase modulated our light with a sinusoidal tone. It is used to obtain sidebands for frequency calibration (normally use 50MHz) to acquire the FWHM in terms of frequencies. The expression of Lorentzian and FWHM can be demonstrated in the following form:

$$\begin{aligned}y &= \frac{1}{1 + (\frac{x - x_0}{\Delta\nu_{\mathrm{FWHM}}/2})^2} \\ &= \frac{{\Delta\nu_{\mathrm{FWHM}}}^2}{{\Delta\nu_{\mathrm{FWHM}}}^2 + 4(x - x_0)^2}\end{aligned} \tag{13}$$

Here $x_0$ is the peak position of lorentzian. An example of this calibration method for FWHM will be further introduced in 4.1.3.

### 2.2.3 Finesse

The finesse of an optical cavity $\mathcal{F}$ is a measure for how narrow the resonances are in relation to their frequency separation: a higher finesse means sharper resonance peaks. It is defined as the FSR divided by the FWHM of the resonance peaks:

$$\mathcal{F} = \frac{\Delta\nu_{\mathrm{FSR}}}{\Delta\nu_{\mathrm{FWHM}}} \tag{14}$$

This is also how we calculated finesse from experimental data.

People always find finesse very useful because there is a relationship found between finesse and round trip loss. With a lower round trip loss we can expect to see some sharper peaks which corresponds to higher finesse. The relationships between finesse and round trip loss $\gamma$ can be expressed as in the following

equation when round trip loss is very small:

$$\mathcal{F} \approx \frac{\pi}{1-(1-\gamma)^{1/2}} \approx \frac{2\pi}{\gamma} \tag{15}$$

Thus, with our experimental we could use the measured linewidth and FWHM to obtain the finesse using Equation 14. Then with Equation 15, we can obtain the round trip loss of our cavity.

### 2.2.4 Intra-cavity power

The intra-cavity power is crucial for opto-mechanical experiments since we study light field and membrane interactions that in linearized optomechanics the optomechanical coupling rate can be tuned through a coherent drive field, which can be enhanced compared to its free-space value by use of a cavity. Thus a good understanding of intracavity field relations provide us with insights of the optical field strength.

Using the results from Equation 4 we can conclude the intracavity- input power relations as:

$$\begin{aligned} P_M &= E_M^2 \\ &= \frac{4E_0^2 t_1^2}{\gamma^2} \end{aligned} \tag{16}$$

Since finesse is what we usually use in our calculation later, we can get the following formula using Equation 15:

$$\begin{aligned} P_M &= \frac{4E_0^2 t_1^2 \times \mathcal{F}^4}{\pi^2(2\times\mathcal{F}-\pi)^2} \\ &= \frac{4t_1^2 \times \mathcal{F}^4}{\pi^2(2\times\mathcal{F}-\pi)^2} P_{in} \\ &= \frac{4\times\mathcal{F}^4}{\pi^2(2\times\mathcal{F}-\pi)^2} P_{off} \end{aligned} \tag{17}$$

Where $P_{in}$ is the input power of the cavity and $P_{off}$ is the off-resonance in-cavity optical power. For a high finesse cavity , we can get the approximate expression:

$$P_M \approx \frac{\mathcal{F}^2}{\pi^2} P_{off} \tag{18}$$

## 2.3 Losses and beam waist

### 2.3.1 Origins of optical losses

Optical losses like scattering loss, transmission and absorption are important properties for the characterization of our membrane, since it can influence the coupling rate significantly[4]. In this section, we will provide some basic explanations for optical losses happened on the membrane.

After we discovered the round trip loss from our measurements, we can only learn about the round trip loss itself, instead of the value of scattering loss which is what we are looking for. This is because the round trip loss contains 3 parts(here we ignore the absorption for now since we will later find that it is negligible):

$$\gamma = t_1^2 + t_2^2 + \beta \tag{19}$$

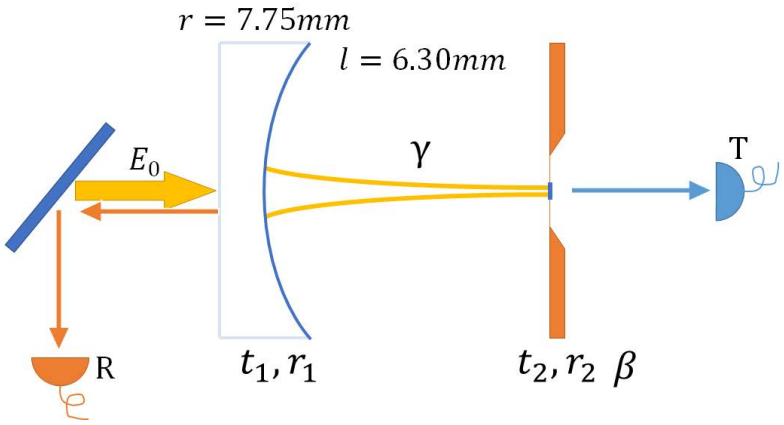


Figure 3: Complete schematic drawing for experiment. The front mirror used on the left is a 500 ppm or 1000 ppm concave mirror with a radius of 7.75mm, and the PhC membrane on the left work as a high reflective back mirror. $\gamma$ is the round trip loss of the cavity, $t_1$ and $r_1$ represent the transmission and reflection coefficient of the input mirror, and $t_2$ and $r_2$ represent the transmission and reflection coefficient of the output mirror(photonic crystal membrane), $\beta$ is the scattering loss on the cavity. We are able to detect the cavity transmission and reflection simultaneously.

Here $\beta$ is the total scattering loss for each round trip. Even if what we wanted to find out was the scattering loss on the membrane itself, for the method we use it is impossible for us to separate all the scattering losses inside the cavity from each other. This means The scattering losses here could come from the membrane or the mirror, but we cannot tell from the data. However, since the scattering loss from a good dielectric coated mirror is very low from the factory data sheet[9], we are safe to conclude that the scattering loss can only happen then the coating is contaminated. In this case can try different concave mirrors

to check how that affects the total scattering loss. If we cannot observe any difference, then it is very possible that almost all scattering losses are from the membrane. In this case, we can establish an upper bound for scattering loss from the membrane is $\beta$. A complete schematic drawing for experiment is shown in Figure 37.

**Scattering loss** It was straightforward to assume that the main contribution of scattering loss came from the clipping diffraction, the contamination on the PhC or the "twisted structures" as we will see later in our observation in subsubsection 3.1.3. However, from the result we obtained in subsection 4.5, this might not be the case.

**Absorption loss** The absorption loss of our $Si3N4$ film can be determined using its complex refractive coefficient[10]:

$$n_c = n - ik \tag{20}$$

Where the real part $n$ is the refractive index and indicates the phase velocity, while the imaginary part $\kappa$ is called the extinction or absorption coefficient. From the data we can see that, with the operation range of our laser(833nm) and a thickness of about $90nm$, the extinction coefficient of silicon nitride is negligible.[11] [12]

### 2.3.2 Gaussian waist

For a certain Gaussian beam that we encountered, its beam waist can be easily determined if we know its waist before entering the lens [13]. The relation is expected to be :

$$2w_0 = \frac{4\lambda f}{2\pi w_0'} \tag{21}$$

Where $w_0$ is the waist at focal point, $w_0'$ is the waist before the lens, $\lambda$ is wavelength and f is the focal length of the lens used to focus the beam.

### 2.3.3 Cavity mode waist

For the scattering losses we mentioned above, the beam size inside the cavity will badly influence our estimated scattering loss and transmission because of the clipping of the PhC defect with the Gaussian beam. Apart from that, normally our membrane is not perfectly fabricated or clean, so an estimated beam size on the membrane will provide us with a good expectation on the losses from the membrane before we even start the measurement, and further benefit

us with the membrane selections before experiment. For example, if we have an PhC membrane with good fabricated area of only 80$\mu$m diameter range, we should not expect small scattering loss for cavity mode that equivalent to a waist $2w_0 > 40\mu m$.

From Figure 1 we know the length of our cavity is 6.30 mm and the radius of curvature for the concave mirror is 10mm. Thus, we can use the equation 48 from Kogelnik and Li's paper [14] to calculate the beam waist:

$$w_0^2 = \frac{\lambda}{2\pi}\sqrt{d(2R-d)} \tag{22}$$

But this equation in their paper only works in a scenario that the cavity consisted of two concave mirror with identical radius, where d in the equation stands for the cavity length and R is the radius of each mirror. $w_0$ in this equation is the beam waist at the centre of the symmetric cavity.

But if we look at our cavity at Figure 1, it is actually half of a symmetric cavity with the beam waist at the membrane. Here, we can assume a flat wavefront at the membrane. Thus, we can convert the equation above to the one more convenient for us to use:

$$w_0 = \sqrt{\frac{\lambda}{2\pi}\sqrt{2l(2R-2l)}} \tag{23}$$

If we plot a waist-cavity length relation for two radius of curvature we used in experiment(10mm and 25mm), we can have our Gaussian cavity mode waists on photonic crystal side as shown in Figure 4.

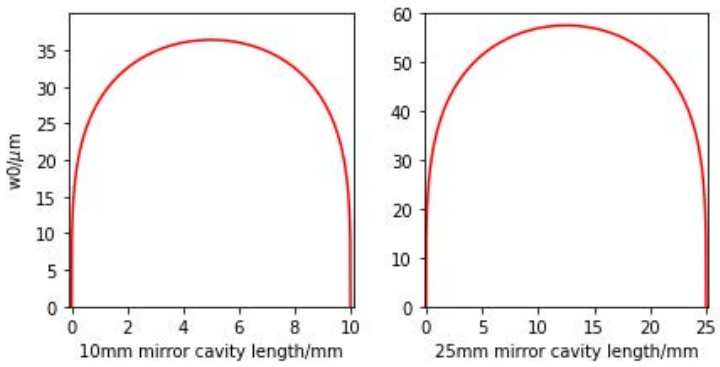


Figure 4: Gaussian cavity mode waists on photonic crystal for two radii of curvature we used in experiment, 10mm and 25mm from left to right.

Here, $l$ is the cavity length we have, equal to 6.3mm. Put our parameters in, we can acquire one of the beam waist of our cavity:

$$\begin{aligned} radius : w_0 &= 36\mu m \\ diameter : 2w_0 &= 72\mu m \end{aligned} \tag{24}$$

## 2.4 MAK cavity coupling discussion

Cavity optomechanics contain two main coupling branches: dispersive coupling and dissipative coupling. [15][16] Both of them have been investigated in the last decade for both optomechanical cavity or cavityless optomechanics. [17] [18] The most common understanding of cavity optomechanics is the so-called dispersive coupling originating from the dependence of the cavity resonance frequency on the position of a mechanical oscillator. In order to fill out the missing part of the coupling story, the so-called dissipative coupling, which can be interpreted in terms of the dependence of the cavity damping rate on the mirror position, is introduced. Since then, manifestations of this coupling have been addressed both theoretically and experimentally[19].

The theory of "Membrane-at-the-back" as an optomechanical system(MAK) developed [20] by Prof. Tagantsev theoretically proved an superior cavity assembly method compared to the so-called "membrane-at-the-edge" system(MATE) and the popular "membrane-in-the-middle" cavity(MIM). In this section, we will briefly introduce the theory and pacing towards the explanation of why the photonic crystal phononic membrane is necessary in the MAK cavity story. All the three methods are shown in the plot below. The content used to be the goal of the whole thesis, but since we will later find out that the membrane mirror quality did not meet the requirement, the contents here are shortened and mainly served as a future outlook.

Here we define several important parameters for the concept of cavity optomechanical system. The single-photon coupling rate:

$$g_0 = \frac{d\omega_{cav}}{dx} x_{ZPF} \tag{25}$$

Where $\omega_{cav}$ is the cavity resonance frequency and $x_{ZPF}$ is the mechanical zero-point fluctuation amplitude, Here $x_{ZPF} = \sqrt{\hbar/2m_{eff}\Omega_m}$, where $m_{eff}$ is the effective mass of the membrane and $\Omega_m$ is the mechanical frequency of the membrane.

From the single-photon coupling rate, we can define the commonly used single-photon opto-mechanical cooperativity rate of the system[21] [22] [23]:

$$C_0 = \frac{4g_0^2}{\kappa\gamma} \tag{26}$$

Here $\kappa$ is the optical decay rate of the opto-mechanical cavity system and $\gamma$ is the mechanical friction rate of the system. The cooperativity here describe how strong the overall opto-mechanical coupling is.

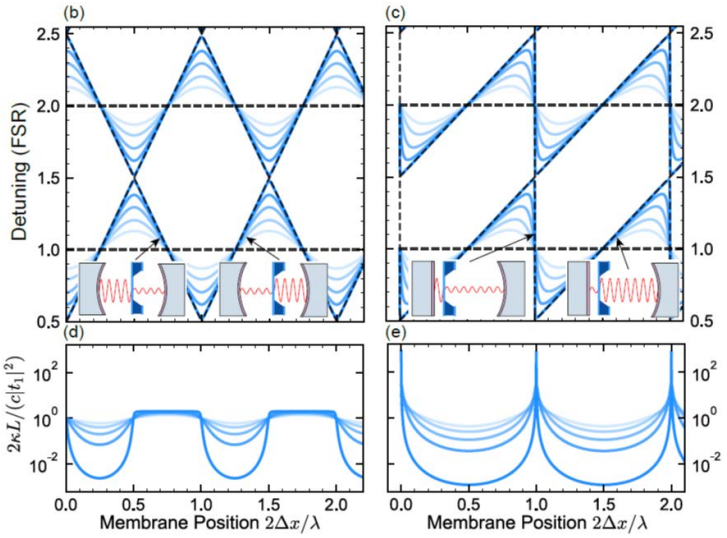


Figure 5: Optical resonances for a membrane in a cavity. This resonance picture is borrowed from the work of Dumont[24]. Optical resonances for a membrane in a cavity. (b)-(c) Dependence of the cavity resonance's detuning (normalized by the free spectral range (FSR)) on membrane displacement $\delta x$ from (b) the cavity center ($x = L \cdot 2$) and (c) the first mirror ($x = 0$), with rm values (from light to dark) -0.4, -0.6, -0.8, -0.931, and -0.9977 (membrane reflectivity $r_m$'s phase chosen to highlight avoided crossings as in [2]). Horizontal dashed lines represent empty cavity resonant frequencies ($r_m = 0$), while other dashed lines represent the left (negatively sloped) and right (positively sloped) sub-cavity resonances when $t_m = 0$. Insets qualitatively show the field distribution of these modes. (d)-(e) Dependence of cavity's energy decay rate $\kappa$ on membrane displacement $\delta x$ from (d) the cavity center and (e) the first mirror, normalized by the empty cavity value for a single-port cavity ($t_2 = 0$, $r_2 = -1$).

For the MIM and MAK system, as shown in Figure 5 we have the membrane position-frequency relations. From the plot, we can see the reason we desire a high reflectivity membrane is because we can reach a much higher $g_0$ coupling rate compared to a common silicon nitride membrane. This effect becomes more obvious in the case of the MATE or MAK situation, where from Figure 5(c) we can see a very high $d\omega_{cav}/dx$ when the main optical power is at the small sub-cavity. However, from Figure 5(e) we can see a high dissipation when we are at this regime. As for the MAK system, it is the reverse of MATE in that the membrane is closer to the back mirror(low transmission mirror). Furthermore, this system will result in a lower optical loss when the main optical power is at the small sub-cavity.

# 3 Early cavityless test and membrane inspections

In this section, the membrane inspection results will be demonstated and explained and the early experiments without a cavity will be briefly introduced.

## 3.1 Membrane inspections

### 3.1.1 Phononic structures and effective mass

The membrane we are using are designed and fabricated by student Yeghishe Tsaturyan who used to be a PhD student at Niels Bohr Institute. His work on ultracoherent soft-clamped mechanical resonators for quantum cavity optomechanics[25] is now widely used in optomechanical experiment here in QUANTOP. For optomechanical experiment, this phononic design is crucial for the reason that it can relate optical and mechanical resonance. The silicon nitride phononic structure design we used in is shown below in Figure 6.

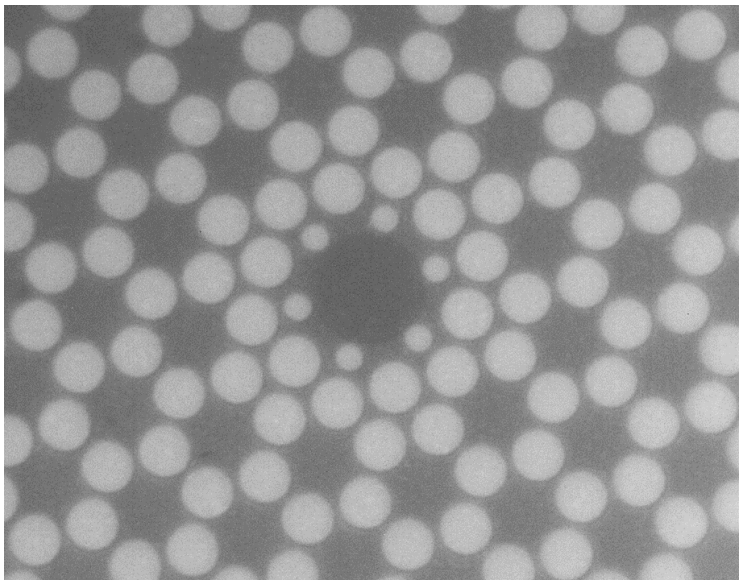

Figure 6: Phononic structure image. The center dark circle(defect) is where the Photonic crystal located.

The phononic structures are used to create a mechanical bandgap to reduce the damping effect of the soft-clamping oscillator. While the center dark cirle is where the photonic crystal located and the place our light-matter interaction will happen. The region always looks dark under a microscope with a back light source, since the photonic structures prevent illumination from going through it.

The effective mass of this certain structure can be calculated using COMSOL multiphysics. We can conclude the effective mass using the following definition:

$$m_{eff} = \rho \int (\frac{|Q|}{|Q_{max}|})^2 \times dV \tag{27}$$

Where $m_{eff}$ is the effective mass, Q is the out-of-plane displacement for a given vibrational mode. From COMSOL simulation, we can only simulate the center defect as a full silicon nitride plate for computing power reasons. Thus the full mystery cannot be disclosed until we have a better understanding of our defect.

### 3.1.2 Mechanical Quality Factor

In physics and engineering, the mechanical quality factor (or Q-factor), is a dimensionless parameter that can be used to describe how underdamped an oscillator or resonator is. It can be approximately defined as the ratio of the initial energy stored in the resonator to the energy lost in one radian of the cycle of oscillation. Q factor is alternatively defined as the ratio of a resonator's center frequency to its bandwidth when subject to an oscillating driving force. For example, a higher Q correspond to a lower energy loss rate and from the oscillations we can see that it will last longer, and vice versa.

Thus, if we have a pendulum suspended from a high-quality bearing, oscillating in air, has a high Q, while a pendulum immersed in oil has a low one.

There are two definitions for this quality factor:
One of these definitions is the frequency-to-bandwidth ratio of the resonator:

$$Q = \omega_m / \Delta\omega \tag{28}$$

The other definition is called the energy dissipate definition, which is what I am going to use in this report:

$$Q = 2\pi \times \frac{energy\,stored}{energy\,loss\,per\,cycle} \tag{29}$$

These two definitions are equivalent in conception, even though in reality, normally one of them will be easier to measure than the other one. In our case, we are very hard to measure $\Delta\omega$ during the experiment, but from what we are going to show for ringdown measurements, we can measure and calculate the energy dissipation.

**Stimulation and Ringdown Measurements** If we want to use the second definition above to measure the decay of oscillation energy, we must first provide the membrane we want to measure with enough energy. This is why we need a stimulation to make the membrane start oscillating.

There are many ways to provide this stimulation, but the two major ways are: using piezo next to the membrane to provide an vibration of certain frequency, or using laser to stimulate the oscillation. Here we used the stimulating laser

because it gives direct force to the center of membrane while the piezo cannot.

We know the momentum of light is very weak, even compare to the nano-membrane. And from classical physics, we know that if we want to oscillate a heavy object with a weak force, what we can use is by resonance. This is exactly what we are trying to do here: we use the stimulation laser to provide a periodic force on the membrane, with the same frequency as the inherent frequency of the membrane, there will be resonances and the mechanical oscillations will keep increasing.

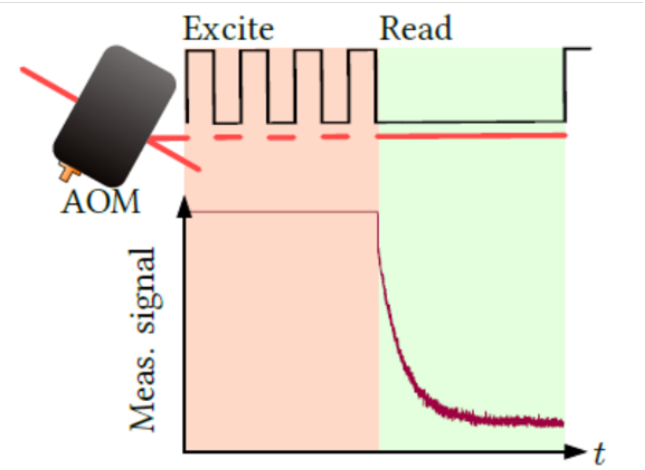


Figure 7: Illustration figure of how stimulation laser works, borrowed from the PhD thesis of William Nielsen, page 111[26]. As we can see from the red part of the red part of the figure, we make the excitation laser go on and off periodically at certain frequency to provide the resonance. After the signal reach the value we want, we can shutdown the stimulation and do the measurements of how fast the decay is (Q-value).

As shown in Figure 7, we can use an AOM with TTL control to make the laser go on and off. In this case, there will be a square wave of momemtum acted on the membrane. If this frequency matches with that of the membrane, we will see the amplitude of the signal we received keep rising.

If we want to measure the Q-factor, we need to shutdown the stimulation, then because it is a damping oscillation, we expect to see a exponential decay as shown in Figure 7. The signals we are measuring here is actually the amplitude of peaks from our stimulation light, which correspond to the oscillation energy of the membrane. The expected form of the decay function should be:

$$A(t) = a \times e^{-bt} \tag{30}$$

Where we know $a$ is the initial amplitude and $b$ can be defined as amplitude

ringdown time. We can thus deduce the Q-factor has the expression of :

$$Q = \frac{\omega_m}{2b} \tag{31}$$

**Q-factor results** The result we measured using ringdown measurements are demonstrated in Table 1. This work is mainly contributed by Jonas Mathiassen and Georg Enzian.

| Membrane number | Frequency(MHz) | Quality factor(M) |
|---|---|---|
| 2 | 1.310 | 0.8 |
| 7 | 1.304 | 15.00 |
| 8 | 1.303 | 24.05 |
| 10 | 1.316 | 23.81 |
| 11 | 1.321 | 24.23 |

Table 1: Some of the quality factor results using ringdown measurements. The membrane we mainly use for our investigation is membrane No.11.

### 3.1.3 Photonic structures and imperfections

The fine photonic structures can be observed and measured under a electron microscope as shown in Figure 8. The summarized measured data can be seen in Table 2.

| value type | designed parameters | real parameters |
|---|---|---|
| thickness | 100nm | 88.5nm |
| lattice constant | 734nm | 728nm |
| lattice hole diameter | 511.2nm | 511nm |
| Photonic crystal size | 200$\mu$m | 200$\mu$m |
| Peak wavelength | 852nm | 833nm |

Table 2: Designed parameters and real parameters of photonic structures. We can see a very clear difference here. The real parameters here were measured by Anders Simonsen via electron microscopy.

When we put our membrane under a 50x optical microscope, we can notice two types of imperfections on our photonic crystal, as we can see in Figure 9. These two types of imperfections, let us call them twisted structures (Figure 9b) and particles (Figure 9c) are observed in almost every single photonic crystal membrane we examined far with very few exceptions.

The origins of the twisted structures remain unknown so far, but we have evaluated their contributions to scattering loss in section 4. It turned out the twisted structures are more destructive to the membrane because when the lattice structures are twisted, they are basically no longer functional at our target frequency. We can see this effect very clear in Figure 9a when we shine a Gaussian beam with a $2w_0 = 100\mu m$ diameter onto the whole membrane, those "leaking" holes are the twisted structures. Ideally in experiment, we should try to avoid those

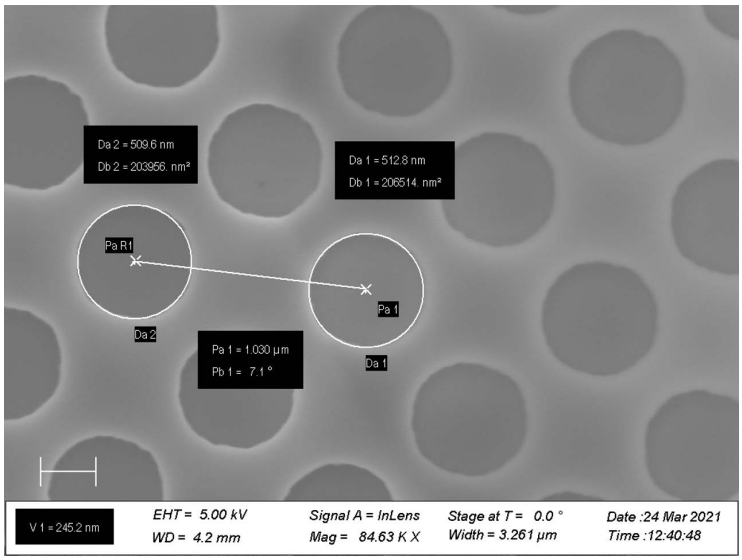


Figure 8: Photonic structure image.

areas. The size of twisted structures are typically around 5-10 $\mu$m.

Another observation was done under the electron microscope about how the "holes" shown in Figure 9(b) looks like with a higher resolution in Figure 10. From the eletron microscope image, we can deduce that the "twisted" structures were actually some blockage in the photonic holes in a certain area, that lead to the malfunctioned photonic holes that caused higher transmission. The explanations for this kind of imperfections in fabrication side remain unknown so far.

The "particles", referring to all the small dots under the microscope that have size around 1 $\mu$m. This kind of contamination is quite common when the membranes are fabricated thus it is possible to be reduced in future wafers. It is worth noticing that the closer a membrane is located to the center of the wafer, the cleaner it is in terms of contamination. The imperfections observed on the membranes for a wafer is shown in Figure 11. From the figure we can see that the membranes at the edge are more likely to be contaminated, but this phenomenon should be further investigated by new wafers before conclusions are drawn.

## 3.2 Early test results

### 3.2.1 Setups and methods

Since the membrane mirror reflects light due to the fact that it contains photonic structures at the center of its phononic structure as shown in Figure 6, a reflectivity-wavelength relations should be expected. A peak reflectivity should

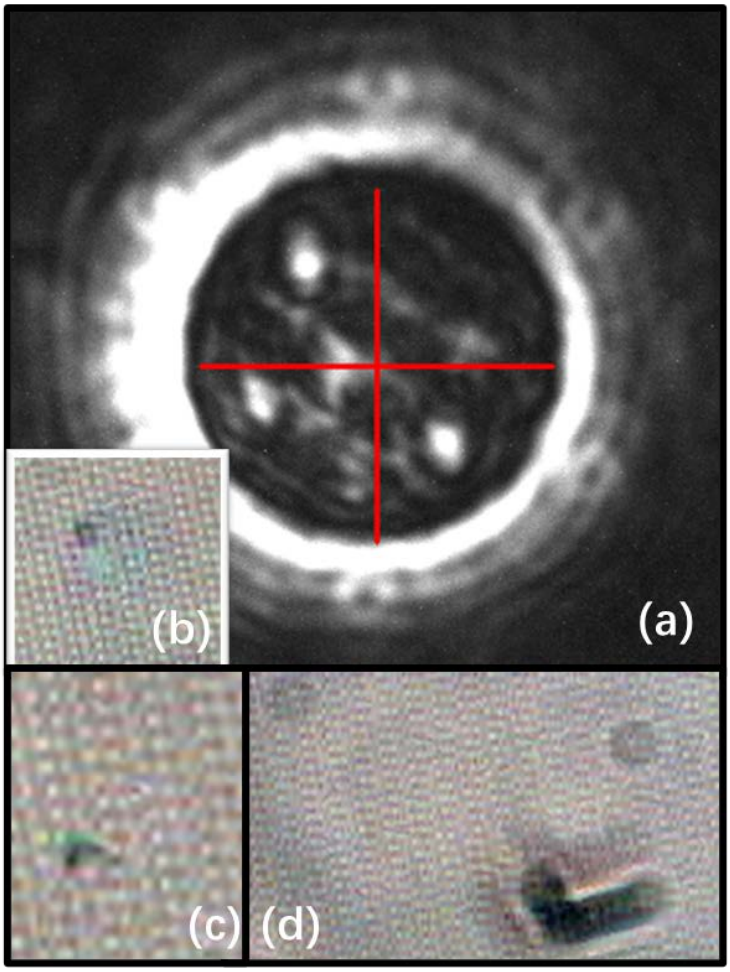


Figure 9: Images about two types of imperfections on membrane. (a) The image of imperfections when we shine a 833nm Gaussian beam on the membrane, and "leaking light" holes are observed at the twisted structures. (b) one of the twisted structure under 50x microscope. (c) particles observed on the membrane under microscope. (d) We can see many other dark shades under microscope, but they are dirts on he microscope instead of membrane. This can be easily verified by simply moving the microscope.

in principle appear at the design frequency of the photonic structure, even though this is rarely the case due to the imperfections of fabrication.

In order to get an overview about how the reflectivity changes in a wider wavelength range, we summarize a typical setup as shown in Figure 12 The setup has three photodetectors: the calibration detector worked as a calibration arm is necessary because we observed some severe polarization fluctuations at the fiber output that caused power fluctuation at the polarizer. And we can get the calibrated power dividing by the calibration signal.

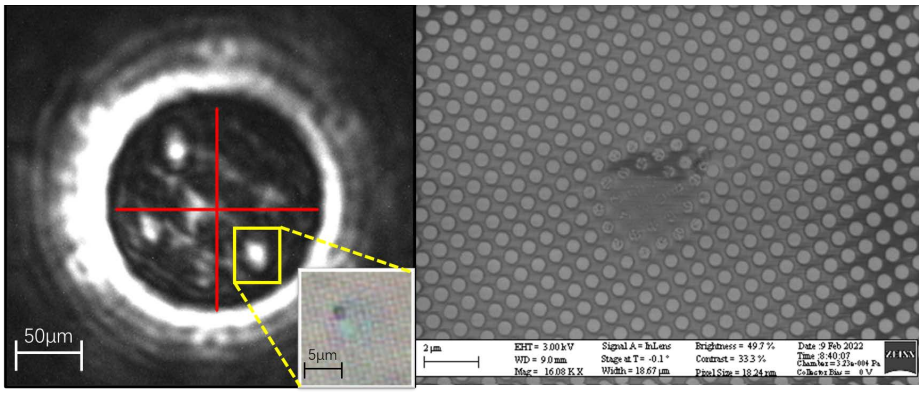


Figure 10: A deeper look into the "twisted structures". It is shown that in the image, the twisted structures are more likely to be air holes blocked by contamination or scratches.

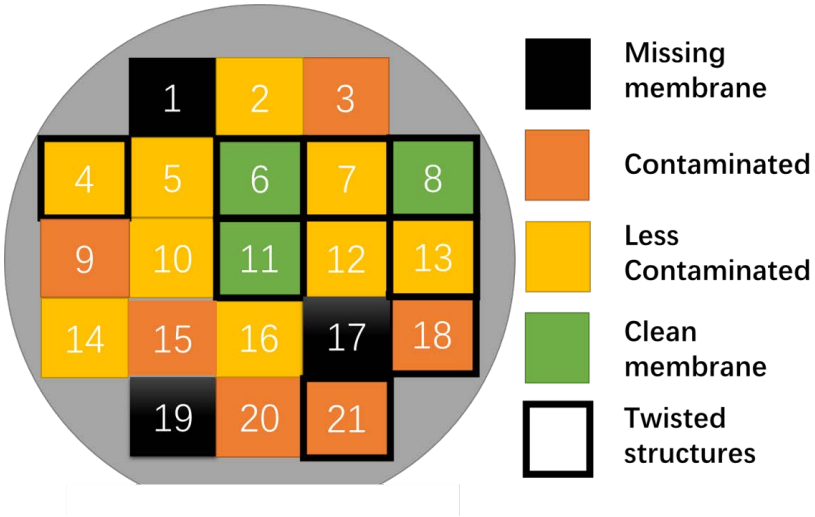


Figure 11: Membrane imperfection status for wafer 1 PhC.

**Calibration tricks** Here we encountered a interesting minor effect that we could not change the height displacement d of light reflected from the membrane using just the 45 degrees positioned mirror in Figure 13, under the condition that the distance of mirror and lens is very similar to the focal length and the input horizontal light is already well aligned horizontally. As shown in Figure 13, green light indicate B-light (Before we moved the mirror), orange indicate A-light(After we moved the mirror by a small angle). If $l_1$ and $l_0$ is similar then no matter how much we move the mirror we can barely affect the height of the reflected light. The reason this effect happened was because when $l_1 = l_0 = f$, the green and orange light path became parallel to each other after the lens and reflected. This corresponds to equal horizontal displacement for green and

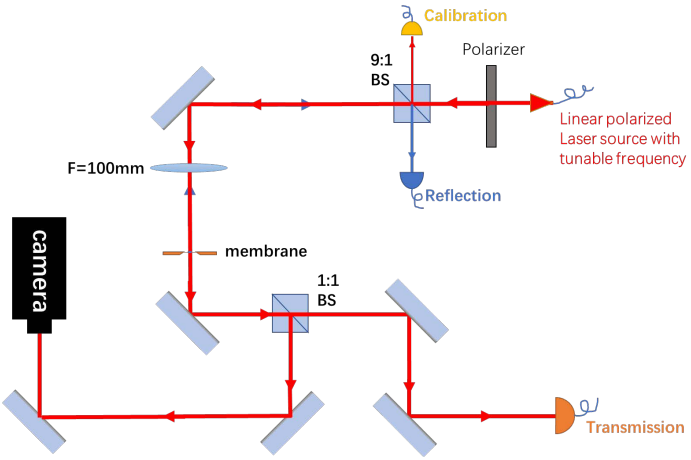


Figure 12: Early setups for cavityless measurements.

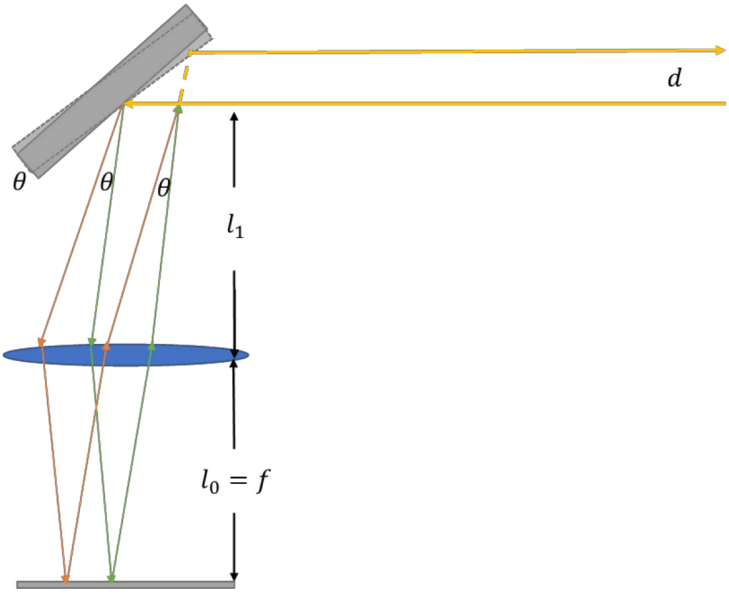


Figure 13: The reflection alignment is impossible when the lens locate at the midpoint.

orange light path after the light is reflected. Thus, we should expect they go back to almost the same point on the mirror as shown in the figure. Thus the vertical displacement d remains roughly the same no matter how we change the angle of the mirror.

**Beam waist on membrane** The beam waist on membrane can be determined using Equation 21, and with the fact that the beam waist($2w_0'$) before entering the lens is 2.5 mm. The beam waist($2w_0$) on the photonic crystal is then 21$\mu$m.

### 3.2.2 Results and limitations

After we successfully coupled light to all photo-detectors, we can start measuring the membrane reflectivity and transmission at different wavelengths. From Figure 14 we can observe a peak reflectivity at around 833nm that reached 95%.

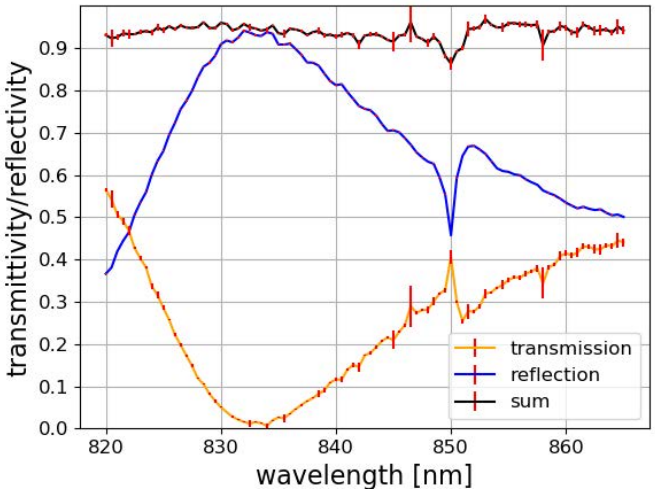


Figure 14: Early results for membrane reflection and transmission.

This measurement is in fact very limited with low result accuracy.

First, when we focus our Gaussian beam onto the 200$\mu$m size photonic crytal using lens is not at all easy, even with a camera in use. This could result in some weak clipping effect at the edge of the photonic crystal that can lead to some extra scattering loss.

Second, the scanning range is 820nm-865nm that some wavelength dependent optical effects may no longer be negligible. All the optical elements on the beam path, for example lens, beam splitters, mirrors they all contain some change of properties when we tune the laser in this relatively large range. Thus, some systematic errors are totally expected.

Third, the beam size here is still small that might have some influence on our outcomes. This effect will be further investigated in section 7.

# 4 Cavity experiments and data analysis

After we have finished the first part of measurement, we realized that in order to reach higher measurement precision, an optical cavity is needed. The cavity measurement is superior to the measurements we did in the last chapter, since the cavity linewidth can be a powerful and accurate tool to obtain the round trip loss[27]. Apart from that, we can also create a better vision from the camera image to help us determine the size of the beam on membrane. This is due to the fact that the intracavity power for our high finesse cavity is orders of magnitude higher than the input power, thus we can physically acquire image from the camera with much higher contrast.

The cavity we used is shown in Figure 15. A complete sketch of the experimental setup of optical path is shown in Figure 17.

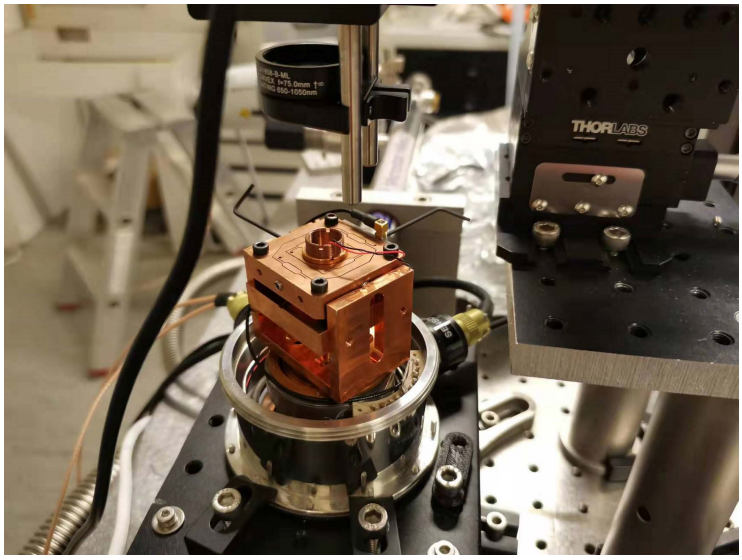


Figure 15: Cavity used for membrane characterization. The light comes in from above and there is a hole in the middle of the stage below cavity, which let through the transmission light of the cavity to the photo-diode detector. There are several degrees of freedom for the alignment of the cavity: top mirror x-y stage controled by two little screw drivers in the picture; stage x-y movement; beam direction controlled by a mirror on the top of the cavity; lens height controlled by moving the lens as well as a fine adjustment by changing the height of stage.

In this section, I will try to provide a clear picture about what I did during the measurements, the alignment techniques and how I acquired and calibrated my data.

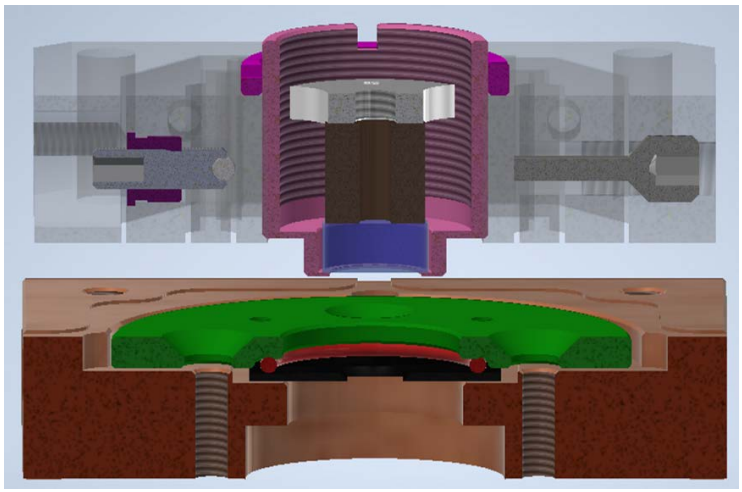

Figure 16: Sketch of cavity setup. The cavity contains a piezo(black) on top of a concave mirror(blue) which is movable in x-y plane. The black wafer at the bottom is a holder of the membrane shown in plot c. The cavith length is determined by the thickness of the green spacer. Red ring in the sketch is a rubber ring which provides frictions for black spacer. In our experiment, the light enters from above.

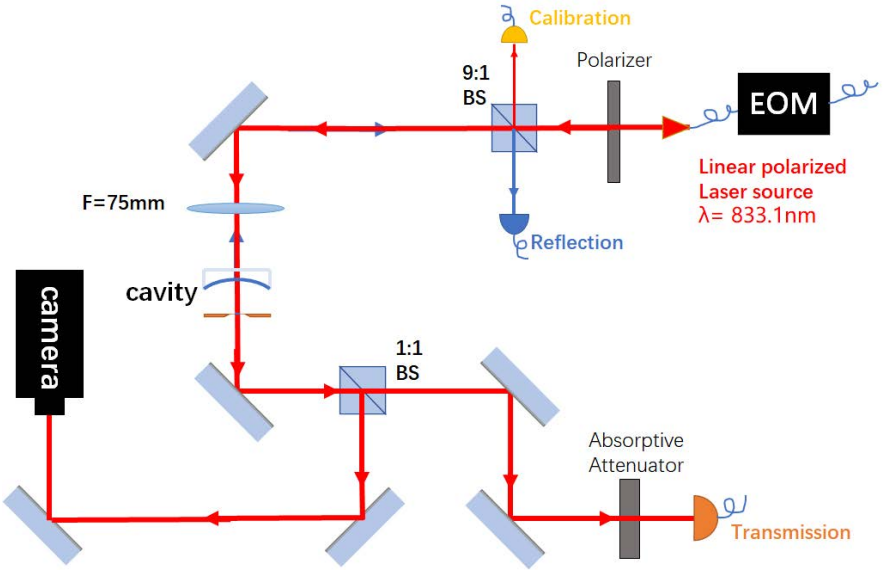


Figure 17: Sketch of the optical setup of experiment. The polarized beam comes in from a PM fiber, with a fine tunable frequency, but the range we use is around 833.1nm. The polarizer we use is for adjusting the input power to the cavity. There are three photo-diode detectors we use: the yellow one is for calibration of the power fluctuation of the input beam; the blue one is for the cavity reflection detection; the orange one is for the cavity transmission detection.

## 4.1 Calibrations methods

There are three different methods I used in the experiment in terms of calibrations. They are aiming for the calibration of power fluctuation (yellow photo-diode detector in Figure 17), 100% transmission for the cavity, and using the Electro-Optic Modulator(EOM) to calibrate the FWHM mentioned in 2.2.2.

### 4.1.1 Calibrations of Power

Since the laser we used came from an external source, there are always some thermal or mechanical fluctuations happening to the fiber[28], that could lead to some polarization uncertainty at the output. By using the polarizer, we can both control the input power to the system and translate the polarization fluctuations to power fluctuations. And by using the 90:10 beam splitter and the calibration detector, we can acquire the fluctuations of power proportional to the power into the cavity. Thus, we can divide them to cancel out the power fluctuation:

$$\begin{aligned} TransmissionSignal &= \frac{Power_{transmission}}{Power_{calibration}} \\ ReflectionSignal &= \frac{Power_{reflection}}{Power_{calibration}} \end{aligned} \tag{32}$$

Note that the signal here is merely a number without any unit, but this is sufficient for us to complete the experiment.

### 4.1.2 Calibrations of transmission

The second part of our calibration is to acquire the 100% transmission signal. I achieved this by getting a calibration signal first when I removed the cavity. And then by comparing the two signals we have the real transmittivity:

$$T = TransmissionSignal/NoCavitySignal \tag{33}$$

The reflection, on the other hand, can be determined without any calibration because it is possible to determine the 100% reflection by just looking at the off-resonance value. The off-resonance reflectivity is approximately 100% because the input mirror has a very high reflectivity of 99.9%. We know that when our cavity is off resonance, the intracavity power phase relations for each round trip is washed away as we discussed in subsubsection 2.2.4, thus we should expect a power inside the cavity orders of magnitude lower than the input beam. Thus, there is near zero destructive phase interference for the reflected beam. We can observe this value in Figure 25

Note that one should always realign the coupling into the transmission photo-diode detector after one removes that cavity or puts it back. Because the cavity,

like other optical elements on the beam path, might shift the beam center a little bit.

### 4.1.3 Electro-Optic Modulator

The Electro-Optic Modulator(EOM) is often used to calibrate the linewidth of a spectrum. EOM is widely used in optical research, thus I will only briefly introduce the EOM I used based on our experiment.

In our experiment, we use a fiber-coupled EOM to insert it between fibers, this kind of EOM looks like Figure 18.

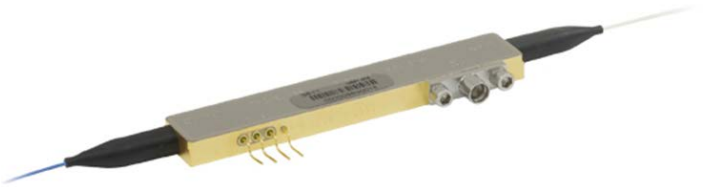

Figure 18: Electro-Optic Modulators, Fiber-Coupled from Thorlab.

As already shown in Figure 17, our EOM is inserted between the input fibers. The EOM can modulate the input light to create side-bands at certain frequency offsets from the carrier frequency. This enables us to control the calibration side-band frequencies and calibrate the FWHM values. It is almost impossible to tell the linewidth directly from the raw data without this kind of calibration.

As an example, when we apply some reference signal on the EOM, the electric signal with a certain frequency $f$ (normally we use 50MHz) will be translated to the spectrum by frequency shifts from the fundamental peaks. Thus, we know that we can calibrate the full width at half maximum by simply using the neighbour side bands. As we can see in Figure 19, the two side-bands are 50MHz from the main peak each. In this case, as we can measure the distance the two side bands from the main peak $\delta x$, and we can also use fitting method in python to acquire the relative FWHM a of the main peak. It should follow the equation below:

$$\Delta\nu_{\mathrm{FWHM}} = \frac{f \times a}{\delta x} \tag{34}$$

## 4.2 Alignment

After the setup is prepared in as shown in Figure 17, we are ready to prepare the cavity to the correct position. The alignment is essential if we want our beam to couple into the fundamental mode. It is not a trivial task to do, so I

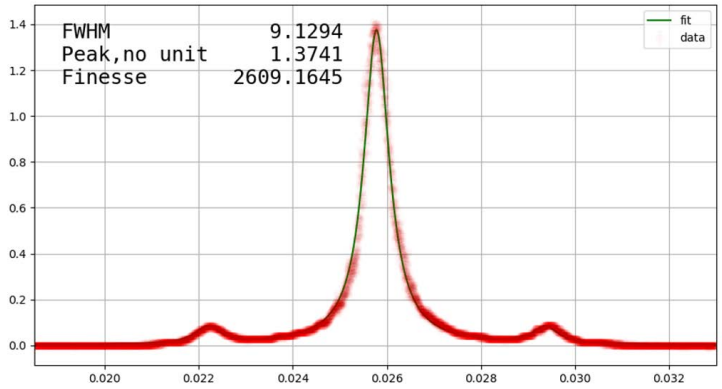


Figure 19: The EOM creates two side-bands next to the main peak, which enable us to calibrate the frequency axis acquired from the oscilloscope in order to obtain the true value for the full width at half-maximum.

am going to separate the alignment into three major steps.

### 4.2.1 Beam-defect alignment

The first step is to look at the displacement of the beam spot from the defect on the membrane by shining a white light into the cavity, and looking at the output side through the camera. By block and unblock the laser, together with the freedom of moving the x-y stage, we can roughly overlap the beam with the defect. We can therefore see the membrane under white light as shown in Figure 20. But once the beam is successfully overlapped with the defect, we will not be able to see it very clearly because of the low transmitivity of the photonic crystal.

Since the flash light we use has board-band frequency range differ from the 833nm infrared light for the actual experiment, it is entirely possible that there are a small misleading displacement between the flash light image and 833nm image. This would result in misalignment if we do not put that into account. Thus, after we roughly align the defect and the beam, we can use a unfocused beam to "image" the membrane, as demonstrated in Figure 21. This is quite useful because we can see the less transmissive photonic crystal(black circle) very clearly. If we use our marker(red cross) to mark down the position of the defect, it is the most accurate result we can ever get.

After we finished those steps, we can turn on the piezo to scan the cavity length. From optics we know that, we should be able to see some moving fringes when we change the cavity length. When we are able to observe this phenomenon, we are ready to move on to the next step.

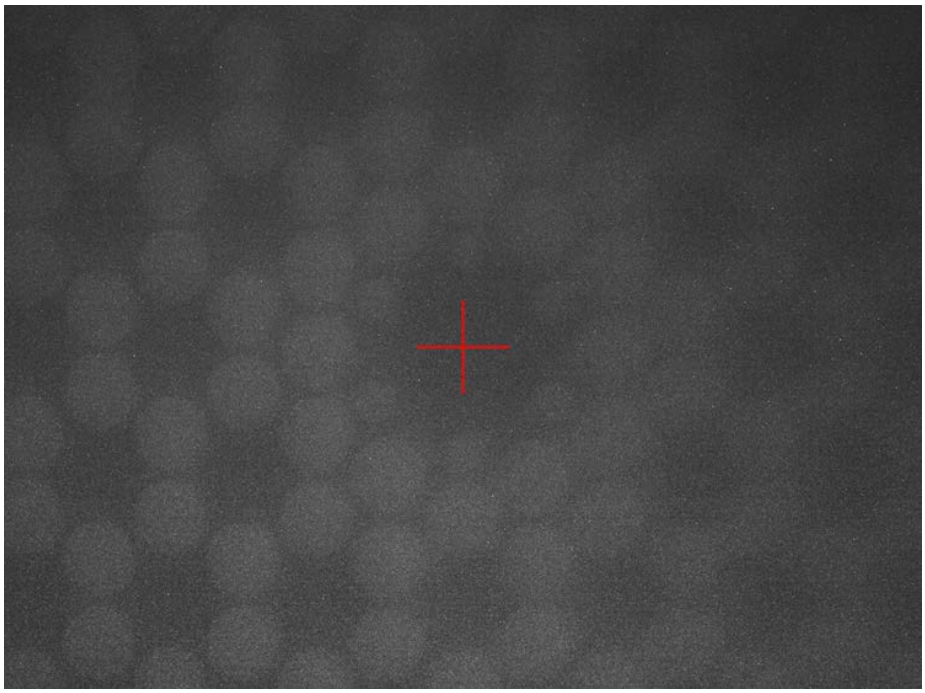

Figure 20: Membrane and defect under the flash light. The black center is where our photonic crystal(defect) is located. A red cross is drawn on the camera to gives a approximate location of the defect.

### 4.2.2 Beam walk

After we successfully overlaps the defect and the beam with each other, we need to put the beam at the correct angle, which is perpendicular to the membrane. And also adjust the distance between the lens to the cavity to get the highest possible in-coupling rate.

I recommend doing it in the following order:

1. Adjust the lens height roughly until there is no visible light in the camera.
2. If the in-coupling angle is too far from right angle, we can observe multiple beam spots on the camera. Beam walk by adjusting the x-y stage and the mirror above the cavity to get it to the right angle, while still have the beam center overlapping with the defect. Keep doing this until all the spots are overlapping with each other.
3. Look at the transmission signal on oscilloscope to search for peaks, until we get the highest possible fundamental mode peak. Fundamental mode can be checked by looking at the transmission beam shape on the camera.
4. Change the fine adjustment of the height of the stage to achieve the best possible fundamental peak.

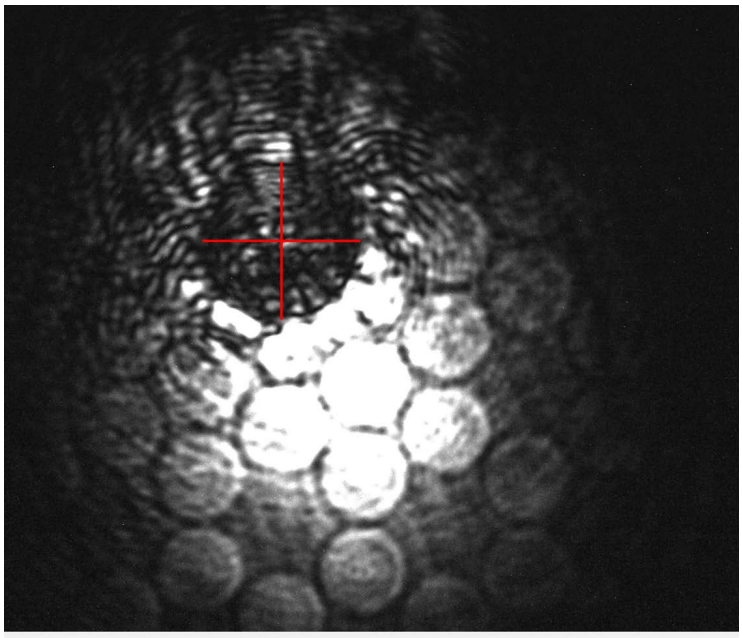

Figure 21: Membrane and defect under a broad waist 833nm laser light. The black center is where our photonic crystal(defect) is located.

#### 4.2.3 Concave Mirror Alignment

After a nice fundamental mode peak is observed, we might still want to move our beam to a better location on the membrane to avoid some high scattering areas, while still keeping the right angle. We can achieve this by only changing the concave mirror x-y position and then stage x-y position.

### 4.3 Measurement methods and early analysis

In order to acquire the proper data for losses and transmission of the PhC membrane we are using, we need to measure multiple quantities. During our experiment, there are four major steps twowards the measurement of all the quantities we need: FSR measurements; FWHM measurements lead to round trip loss; reflection analysis; transmission calibrations and analysis. All these quantities are important for us to further characterize the photonic properties of the PhC membranes we have.

#### 4.3.1 Data acquisition

The optical power data we collected from photo-detector is collected by an 8-bits oscilloscope that is controlled by lab computer. During the experiment, the spectrum is scanned by a small a ring-shaped stack of piezo-ceramic material, forming a piezo-electric transducer that we commonly called “piezo”, as shown in Figure 16. The piezo can tune the cavity length in a small range about 0.5 $\mu$m which is equivalent as a frequency tuning in about 30GHz range(about 1

$\Delta\nu_{\text{FSR}}$ in spectrum). This enable the oscilloscope to capture the certain range we are willing to capture as shown in Figure 19.

After the data points are captured, it is then imported into a python script to process the data. In the python script, we use triple Lorentian to fit the data, as discussed in subsubsection 4.1.3.

### 4.3.2 FSR measurements

As we talked about in 2.2.1, FSR quantity is essential if we want to get the finesse of our cavity and acquire a more accurate cavity length.

The FSR can be acquired when we tune our laser wavelength until the fundamental cavity resonance peak shows up on our oscilloscope again. Or equivalently, we can also use a piezo to tune the length of the cavity until we observe the same peak, but this is less accurate than the previous approach and also requires a good calibration method.

Here we use the first method mentioned above. We can first use the oscilloscope to draw a base line for initial position of the fundamental resonance mode peak. Then, we tuned the laser frequency until the new peak corresponding to another frequency reaches the base line again. In our experiment, since we are aiming at reaching higher accuracy, we keep tuning until the tenth fundamental mode peak reached the base line. And then we can use Equation 12 to calculate FSR.

The result for the 6.3mm cavity is shown in chart below:

| Direction | $\lambda$ /10 FSR | $\delta\lambda$ /FSR | FSR |
|---|---|---|---|
| Increase | 833.000nm to 833.551nm | 0.0551nm | 23.82 GHz |
| Decrease | 833.551nm to 833.000nm | 0.0551nm | 23.82 GHz |

And by using Equation 9 we are able to calculate that the cavity length l is 6.30mm from $\Delta\nu_{\text{FSR}}$ and speed of light. This value is used in advance for both Figure 1 and Equation 24, this is how the cavity length is accurately measured.

### 4.3.3 FWHM measurements and Finesse

After we have the FSR value from 4.3.2, next step we should find a way to acquire the FWHM value as the second step towards round trip loss. After writing a python program to calibrate the power mentioned in 4.1.1 and finish the alignment mentioned in 4.2, we can acquire some really nice Lorentzian peaks corresponding to the fundamental mode. When we zoom in to look at one of them, we will be able to see a good Lorentzian peak as shown in Figure 22. Here, we can easily use a single Lorentzian fit to acquire the height of the peak.

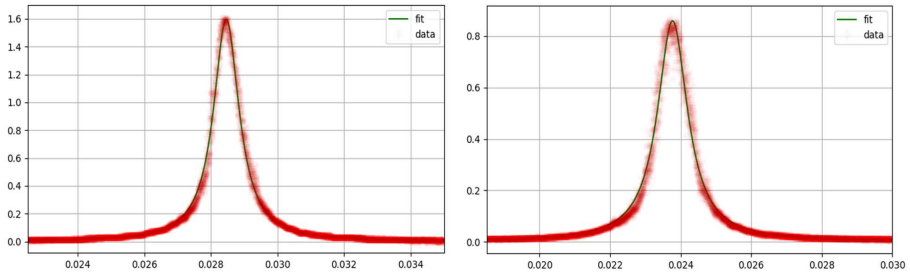


Figure 22: Peak of fundamental mode at wavelength of 833.155nm(left) and 832.75nm(right). The transmission at resonance is 1.59 and 0.87 reading from the plot.

After we applied a 50MHz signal to the EOM as shown in 4.1.3, we can get two other plots Figure 23 and Figure 24 for the FWHM calibration.

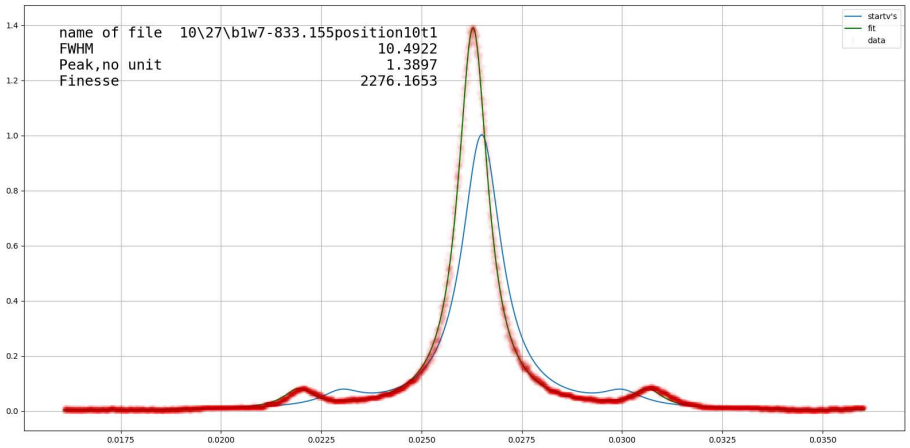


Figure 23: FWHM measurements at 833.155nm. The blue curve in the background stand for the starting value we set for the triple Lorentzian fitting to start.

From these plot we can apply a triple Lorentzian fitting using Equation 13 for three times:

$$y = \frac{a \times {\Delta\nu_{\mathrm{FWHM}}}^2}{{\Delta\nu_{\mathrm{FWHM}}}^2 + 4(x - x_0)^2} + \frac{b \times {\Delta\nu_{\mathrm{FWHM}}}^2}{{\Delta\nu_{\mathrm{FWHM}}}^2 + 4(x - x_0 - \delta x)^2} + \\ + \frac{b \times {\Delta\nu_{\mathrm{FWHM}}}^2}{{\Delta\nu_{\mathrm{FWHM}}}^2 + 4(x - x_0 + \delta x)^2} \quad (35)$$

In the fitting equation, $\delta x$ stands for the distance between main peak and side peaks, while a and b are two vaiables for fitting purpose. After fitting we can

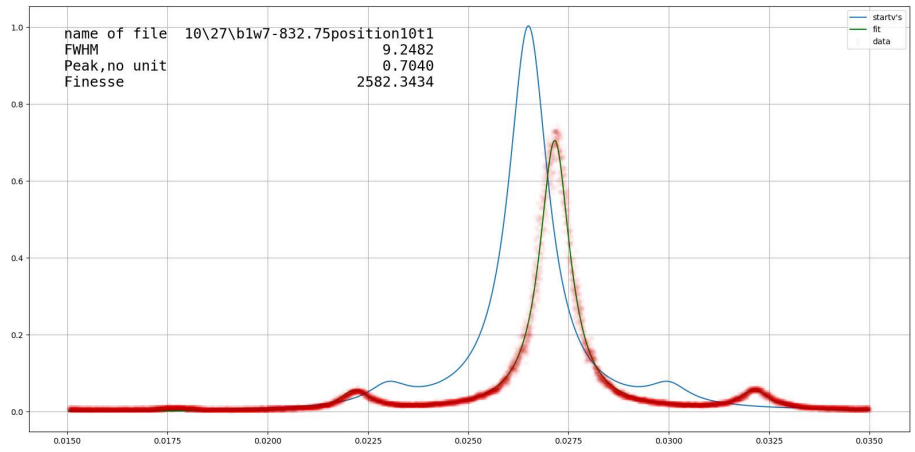


Figure 24: FWHM measurements at 832.75nm.

get the relations between FWHM and $\delta x$. Together with Equation 34, we can get the FWHM value in term of frequencies. Combined with the FSR value we acquired in 4.3.2 and Equation 14, we can get the finesses we always wanted to have, as shown in Figure 23 and Figure 24. Here since from Equation 35 we know that we have 5 different variables to be determined, we need a starting value to do the fitting. In the figures, starting values are shown in blue. We need a proper staring value to make the fitting process nice and quick, normally we plot it as we shown to know how far the starting value is from the actual data (red).

Finally with the finesses we can acquire the round trip loss using the inverted version of Equation 15(we used the first expression for finesse here to acquire better numerical accuracy):

$$\gamma = 1 - (1 - \frac{\pi}{Finesse})^2 \tag{36}$$

Thus, we can get the round trip loss $\gamma$ for each color of input laser:

| Wavelength | Finesse | $\gamma$ |
|---|---|---|
| 833.155nm | 2276 | 0.00276 |
| 832.75nm | 2582 | 0.00243 |

### 4.3.4 Reflection measurements

After we finished the measurement of round trip loss, from what we learned in 2.1, we know that if we can achieve the measurement of cavity transmission and cavity reflection, we will be able to get the data we need.

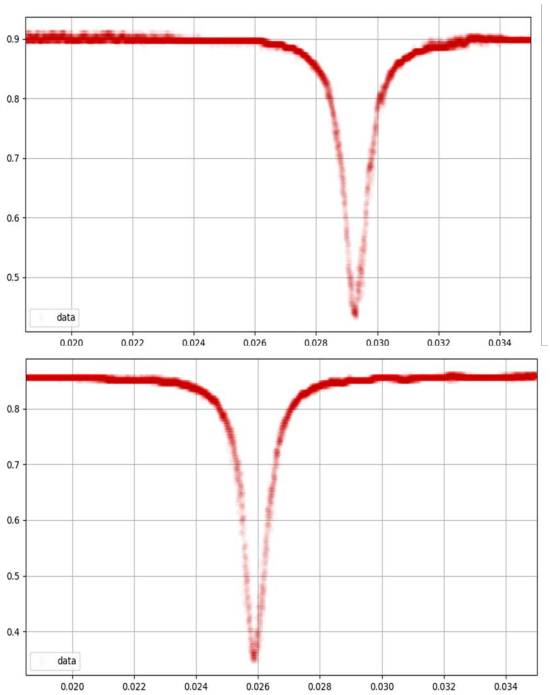


Figure 25: Peak of fundamental mode reflection at wavelength of 833.155nm(up) and 832.75nm(bottom). The transmission at resonance is 0.44 and 0.34 reading from the plot.

In order to receive the real data about reflection, we should always remember to turn off the EOM calibrations first before getting the reflection data. Otherwise, EOM will provide us with a lower resonance peak. Then, we can acquire what is shown in Figure 25.

It is quite obvious for us to tell the 100% reflection value from the plain area in the plot. This is because when the cavity is off resonance, with a 1000ppm mirror it should reflect 99.9% of the input power. Thus, from the two plots, we will be able to get the following values:

| Wavelength | 100% reflection | Resonance reflection | Cavity reflectivity |
|---|---|---|---|
| 833.155nm | 0.91 | 0.44 | 0.48 |
| 832.75nm | 0.87 | 0.34 | 0.39 |

### 4.3.5 Transmission measurements

As we talked about in 4.1.2, in order to measure the transmission, we first need to remove the whole cavity to get the value for 100% transmission. The value we had for transmission is 5.6. Here we should always keep in mind that we probably need to readjust the transmission coupling into the photo-diode detector whenever we move the cavity.

Here are the transmission values we acquired from the peak values read from Figure 22:

| Wavelength | Resonance transmission | Cavity transmittivity |
|---|---|---|
| 833.155nm | 1.59 | 0.285 |
| 832.75nm | 0.87 | 0.155 |

## 4.4 Early result analysis

Combining all the results above and remember in 2.1 we had the relations in Equation 4 and Equation 8, we had four groups of data used to solve the value for $t_1^2$ and $t_2^2$. The reason we need two groups of measurements is that there are always two group of solutions for the transmissions and scattering. Thus, we need to either tune the frequency or walk the beam to some other losses to exclude one solution. I will have a brief example about my assumptions and expectations when using two or more groups of data at different frequencies.

### 4.4.1 Determination of best operational frequency of membrane

One of the crucial parameters we need to determine before we start our measurement is to determine the best operational frequency for our membrane. This frequency is also called central frequency for the reason we will see later in this section. Even though we haven't introduced exactly how we should process the data we acquired above yet, please bear with me for a moment so that we will not have to go through all the back and forth tedious testing in our experiment but use this central frequency later directly to demonstrate how the data is processed.

When we use the method that will be later introduced in subsubsection 6.1.2, we can acquire some membrane transmission data points and then we can find out that they can be roughly fitted into a parabola, as shown in Figure 26. Thus, we can conclude that we have a center wavelength at 833.15nm that gives the lowest photonic crystal transmission we can ever get in all frequency range.

### 4.4.2 Summary of early measurement methods

I obtain the results above using a very early version of group measurement which will be introduced in section 6. The results was obtained with huge error bars as we can see in Figure 26. However, the result is already enough for us to guess the best operation wavelength for our membrane.

After I finished the early measurements discussed above, I then moved to measure the results from some of my better membrane at hand. During the measurement process, we discovered that a proper way to analyse our result is urgent to be developed in order to obtain a good enough scattering loss results resolution.

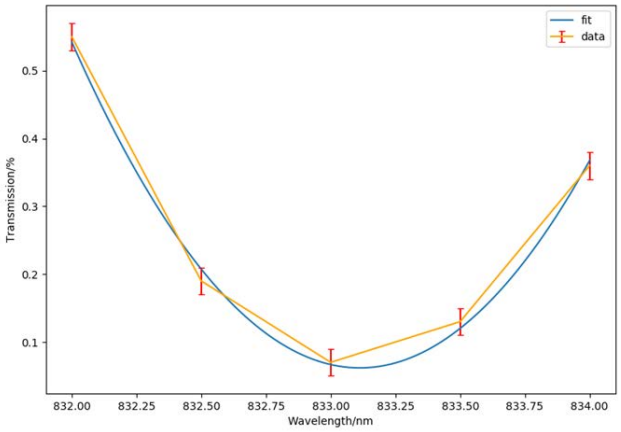


Figure 26: The fitting of different frequencies in order to determine the lowest transmission wavelength.

Thus, we will open a whole chapter to discuss the advantages and disadvantages of all the method that we used.

## 4.5 Results summary

With the improved data analysis method I got some much more accurate results. From there on, more and more new effects are observed and analysed, especially when high finesse is reached with better membranes. These effects will be discussed in section 5.

| **Membrane number** | **Minimum $\gamma$/ppm** | **Minimum T/ppm** |
|---|---|---|
| 2 | 4900±100 | 2500±150 |
| 7 | 1300±200 | 500±170 |
| 8 | 2200±200 | 600±160 |
| 10 | 900±40 | 350±40 |
| 11 | 780±10 | 310±10 |

Table 3: The minimum scattering loss($\gamma$) and minimum transmission($T$) we obtained from our measurements. The membrane we mainly use for our investigation is membrane No.11. Here we used group measurement and its variations to obtain results for 7 and 8. We used earlier pairing method to obtain results for membrane 10, and we used our best approach to obtain results for membrane 2 and 11.

Here is a summary of results acquired with different membranes in Table 3. It is worth noticing that the result we demonstrated here are not obtained using the same analysing method. We will continue our discussion on the topic in section 6.

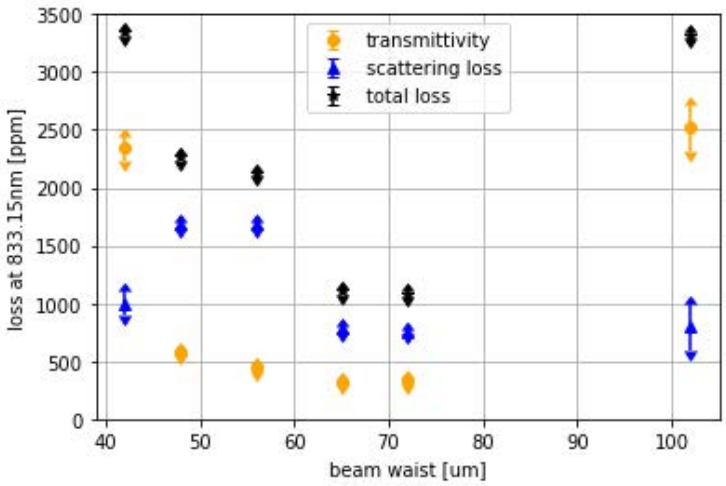


Figure 27: The results acquired by pairing method at different cavity mode waists($2w_0$ at membrane side). We can see that the results at both higher and lower waists contain more scattering loss. The higher transmittivity at $102\mu$m here was due to the power that tails of the mode field lying outside the photonic-crystal region of the membrane received as transmission light at photo-detector.

And in Figure 27, we demonstrate how the transmittivity, scattering loss and total membrane loss are at different beam waists($2w_0$ at membrane side). From the plot we can determine that the best operational waist for our cavity is about $2w_0 = 70\mu m$.

Another interesting fact that we learnt from Figure 27 is that minimum scattering loss did not decrease when we have a smaller beam waist. This fact implies that our earlier intuition about the origin of scattering loss in section 2.3.1 was incorrect. The minimum scattering loss we obtained from membrane 11, independent of its cavity mode interaction area on the membrane and interaction waist, the minimum is always larger than $750ppm$. Thus, this scattering loss should be originated from some more universal fabrication issue.

# 5 Investigations of other effects

After we put membrane No.11 in our optical resonator, many new phenomena emerged and were gradually investigated and understood. In this section, I will introduce some of the key effects of the new membrane, and provide some promising explanations and solutions for them.

## 5.1 Birefringence

### 5.1.1 Birefringence phenomenon

The birefringence effect on a 2-dimensional silicon photonic crystal was observed and studied decades ago on either slab [29] or square lattice fiber[30]. Thus it is not a surprise for us to observe this phenomenon when we use a silicon nitride photonic when our finesse becomes as high as 3000. This phenomenon appeared when we shined a non-linearly polarized light or a linear polarized light with an angle to the lattice direction.

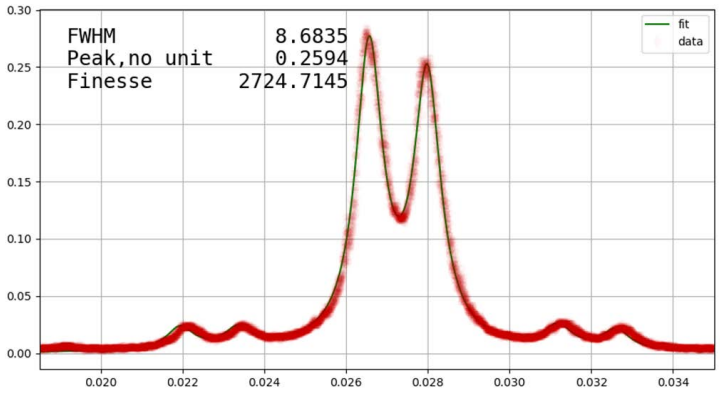


Figure 28: The birefringence effects from the spectrum. We can see that the single peak we observed before splitted into two peaks when we shine a non-linear lattice oriented light into the cavity.

Here, instead of using triple Lorentzian to do the fitting, we need to add other two variables which are: split separation variable d and peak ratio vaiable c that describe a duplication of the triple Lorentzian but can change the frequency differences and heights. Thus, we can fit all six Lorentzian peak using the following equation:

$$y = \frac{a \times {\Delta\nu_{\mathrm{FWHM}}}^2}{{\Delta\nu_{\mathrm{FWHM}}}^2 + 4(x - x_0)^2} + \frac{b \times {\Delta\nu_{\mathrm{FWHM}}}^2}{{\Delta\nu_{\mathrm{FWHM}}}^2 + 4(x - x_0 - \delta x)^2} + \frac{b \times {\Delta\nu_{\mathrm{FWHM}}}^2}{{\Delta\nu_{\mathrm{FWHM}}}^2 + 4(x - x_0 + \delta x)^2} + \frac{c \times a \times {\Delta\nu_{\mathrm{FWHM}}}^2}{{\Delta\nu_{\mathrm{FWHM}}}^2 + 4(x - x_0 - d)^2} + \frac{c \times b \times {\Delta\nu_{\mathrm{FWHM}}}^2}{{\Delta\nu_{\mathrm{FWHM}}}^2 + 4(x - x_0 - d - \delta x)^2} + \frac{c \times b \times {\Delta\nu_{\mathrm{FWHM}}}^2}{{\Delta\nu_{\mathrm{FWHM}}}^2 + 4(x - x_0 - d + \delta x)^2} \quad (37)$$

Despite the fact that the two peak looks quite identical in terms of line width, we realized there is a small finesse differences between them. This difference is implying that the two eigen-polarizations have slightly different losses and we could in principle always use the one eigen-polarization with higher finesse.

### 5.1.2 Birefringence splitting difference

Here I will show the difference of eigen-polarization splittings for different input polarizations. The separation of peaks can vary when we changes the orientation of our input polarized light. This is verified by a polarizer above the cavity, and shown two 45 linear polarized light provide two different separations of peaks. As shown below in Figure 29, the peak separations in two plots have a separation ratio of 9:11. This is way beyond our measurement error. Apart from the separation ratio, the depth of the dip between the two peaks also indicate that this phenomenon is not measurement errors.

Sadly, the origin of this difference remains unknown so far.

### 5.1.3 The eliminations of birefringence effects and results

Due to all the reasons above, we should send in a linear polarized light, aligned with one of the lattice axis. Thus, as shown in Figure 30we add a halfwave plate and a polarizer before the light get into the cavity. Here, since the mirror and lens can potentially disturb the linear polarized light, the polarizer 2 is added between the lens and the cavity to prevent any elliptical light.

The improvement after the adjustment is made is demonstrated in Figure 31, we can see an improvement of finesse after we eliminated one of the polarizations.

## 5.2 Opto-mechanical bistability

### 5.2.1 Bistability effects and the "jumps"

The optical bistability induced by light pressure has been long observed and studied since decades ago by researchers. In this domain, the first cavity optomechanical experiment demonstrated bistability of the radiation pressure force acting on a macroscopic end-mirror hanged by a string back in 1983. [31] [32] Thus, this phenomenon is expected to be observed by our ultralight photonic mirror hanged by a phononic bandgap structure. However, in the original Dorsel

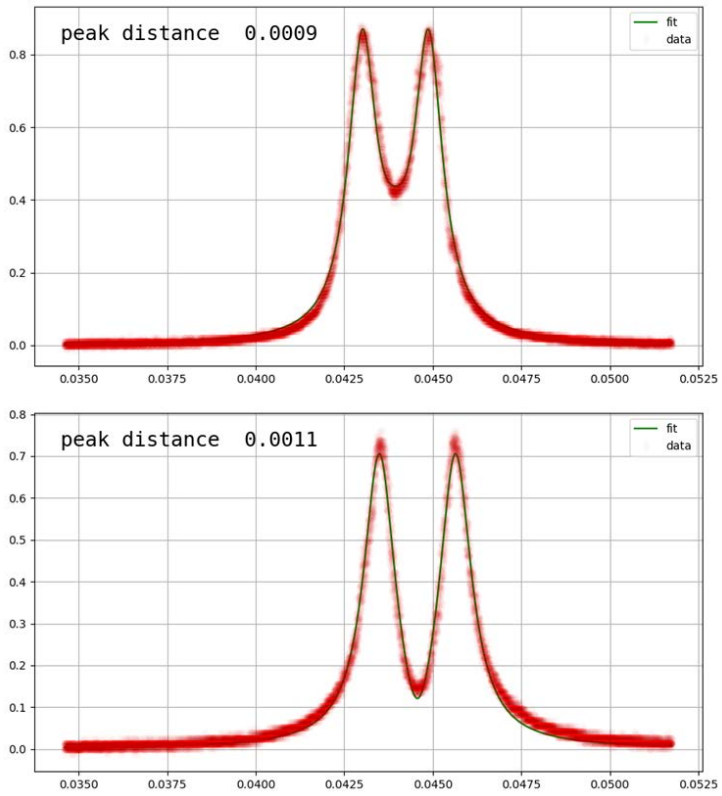


Figure 29: The birefringence effects shows different splittings at plus or minus 45 degrees linear polarization inputs into the cavity. The peak separations in two plots have a separation ratio of 9:11. This is way beyond our measurement error.

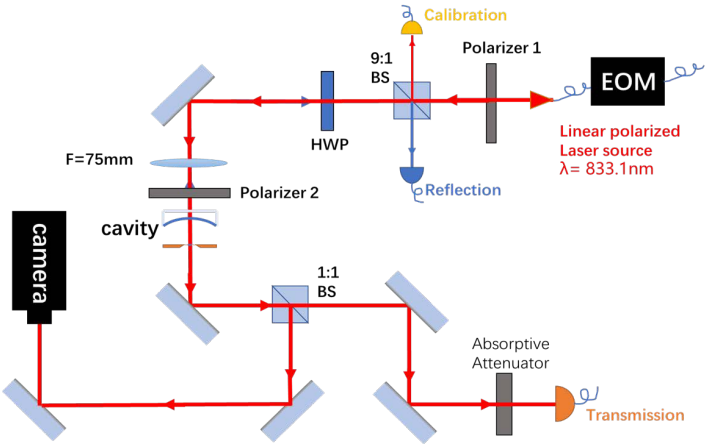


Figure 30: Changes of setup for birefirngence eliminations. HWP and Polarizer 2 are added to provide linear polarization inputs at arbitrary angles.

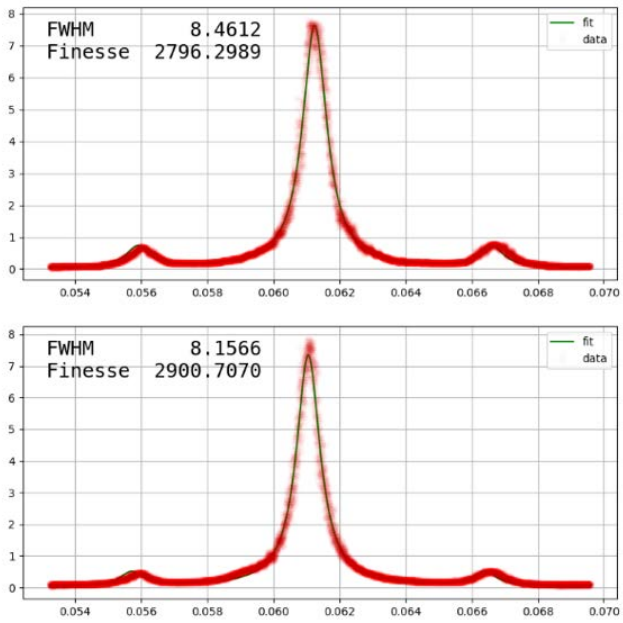


Figure 31: Results comparison after birefriengence elimination. The two peaks have small differences for their finesse, so we always test both polarization inputs and choose the one with slightly higher finesse.

paper they had a hard time to achieve the separation of bistability signals and optical noise. Taking advantage of our advanced membrane mirror, we can see this bistability with a better physical resolution.

This result can be observed in bistable behaviour and hysteresis when recording the circulating photon number $n_{cav}$ or the transmission as a function of laser detuning, as shown in Figure 32 [22]. The bistability occurs when the optical power with position dependence of the mirror create a second minimum potential. Thus, there could be two stable position corrsponded to two different intracavity powers for the mirror for a given mirror position. In our experiment, since we have a cavity with a piezo behind the concave mirror that can tune the cavity length as shown in Figure 16, the expected bistability with a tuning laser should looks like Figure 32(b). However, this plot imply an interesting fact which is there should be a color dependence of the bistability effect when the in-cavity power is high enough. When we are scanning from blue to red and red to blue, two different "jumps" should occur since the actual curve cannot follow the imaginary line in (b), but "jump" straight up and down when it cannot follow the real curves anymore. Thus, the bistability "jumps" are expected to occur at two different frequencies 1 and 2 marked in Figure 32(b). We are also confident to make the prediction that the gaps of the "jumps" vary by our scanning direction. All these phenomenons from theoretical predictions are verified in Figure 32(d), as we can see the asymmetric effect for both frequencies and "jumps". However, a more quantitative calculation should cast light on our

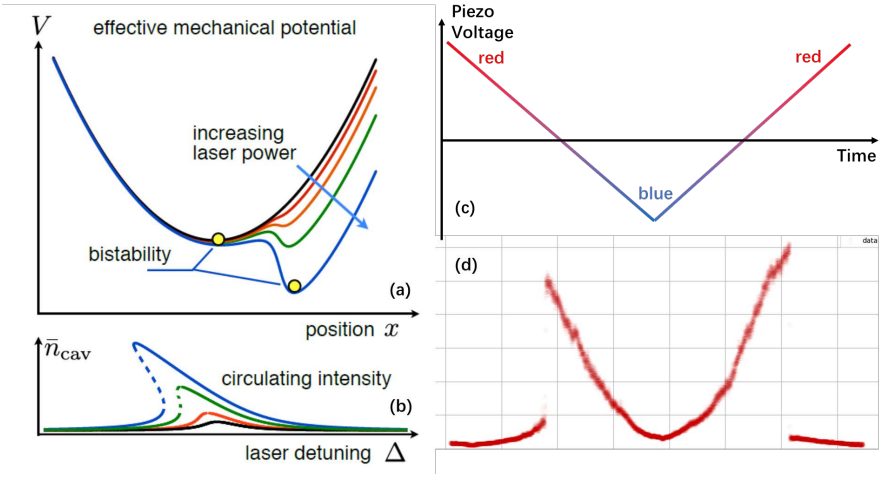


Figure 32: The bistability effect. Here figure (a) and (b) are from cavity optomechanics page 21 by Markus Aspelmeyer [22]. (a) Opto-mechanical bistability effect happens when the optical power with position dependence of the mirror create a second minimum potential. Thus, there could two stable position for the mirror for a given mirror position. (b) Theoretical expectation of the bistability effect when we have a laser detuning or a piezo that can tune the cavity length. (c) The corresponded piezo scan is equivalent to a scan from red(low frequency) to blue(high frequency) and back to red. (d)Spectrum data recorded when we make a full peizo scan period from blue to red(left) and from red to blue(right). The experimental result that we collected which indicate a bistability here, since the two "jumps" happened asymmetrically at different laser tuning frequency and appeared with different heights.

final doubts for the qualitative explanations.

### 5.2.2 Quantitative calculations of bistability effects

In order to calculate our theoretical bistability effect, the optical force is needed for our calculation[22]. After measurement we can get the total input power into the cavity 2.5mW and finesse 2800. Using Equation 17 we acquired, we can conclude that the intracavity optical power is about 2.2 W.

In our case we should consider the optical power as an "optical spring" that follows the overall potential for the mechanical motion also includes the intrinsic harmonic restoring potential:

$$V_x = \frac{m_{eff}\Omega_m^2 x^2}{2} + V_{rad} \tag{38}$$

Where $\Omega_m$ is the mechanical frequency, $m_{eff}$ is the effective mass obtained in subsubsection 3.1.1 and $V_{rad}$ is the "optical spring" optential defined by op-

tomechanics textbook[22]:

$$V_{rad} = -\frac{1}{2}\hbar\kappa n_{cav}^{MAX} \arctan[2(Gx + \Delta)/\kappa] \tag{39}$$

Here for simplicity, we can take advantage of our high finesse cavity to simplify Equation 38. For a 3000 finesse cavity, using Equation 18, we can determine that its on-resonance power and off-resonance power can have a difference of roughly 1 million times. Thus,it is safe for us to ignore the off-resonance optical pushing force and treat the two bistable position as two equilibrium positions of light and no light instead of on and off resonance.

For the on-resonance case, we have 2.2W of power in the cavity. If we see it as a group of photons(n indicates photons per second), we know from textbook that:

$$\begin{aligned} P &= \frac{E}{t} = n\hbar\omega \\ &= n\frac{hc}{\lambda} = 2.2W \end{aligned} \tag{40}$$

Thus, the force exerted onto the photonic mirror can be calculated (here we see the photon collisions on membrane are purely elastic):

$$\begin{aligned} F &= 2 \times \frac{p}{t} = 2 \times n\frac{h}{\lambda} \\ &= 2 \times \frac{P}{c} \approx 15nN \end{aligned} \tag{41}$$

With the results from subsubsection 3.1.1 we can now try to relate everything together using Equation 38 by modelling it as a force pushing a oscillator to reach the second equilibrium:

$$\begin{aligned} F &= k_{eff} \times d = V''_{eff} \times d \\ &= m_{eff}\Omega_m^2 d \end{aligned} \tag{42}$$

Where $V_{eff}$ is the oscillator potential. Recall that we know from our test in section 3.1.2 that for membrane No.11 the drum mode frequency is 1.321MHz from Table 1. Here we can acquire the membrane displacement by optical force:

$$d = \frac{F}{4\pi^2 m_{eff} f_m^2} \approx 0.1nm \tag{43}$$

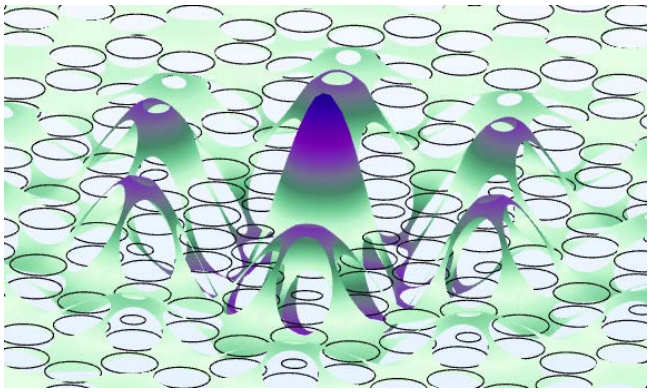

Figure 33: An exaggerated sketch for z displacement of the fundamental phononic mode.

But this calculation method has a fatal error in its calculation! The reason of the incapability of this calculation to provide a reasonable result is because, this calculation can only apply to a certain mode that can be regarded as a simple optical spring. A sketch of the mechanical fundamental mode for the membrane can be found in Figure 33. We can see from the sketch that we cannot get the same displacement distribution when applying a constant force at the center. For our case, the bistability originated from two constant force inside the optical cavity, thus we should do the calculation based on a new COMSOL simulation. Eventually, from a mechanical simulation based on a constant optical force, we obtained a displacemnt of 0.33nm.

From the optical force driven displacement, now we are able to infer the optical frequency displacement that this 0.33nm mirror movement corresponds to. Using the fact that this cavity has a length of 6.3mm and $\lambda$= 833nm. Thus we know from subsubsection 2.2.2 that this displacement above correspond to a frequency change of:

$$\begin{aligned} \Delta\nu &= \frac{\nu dc}{l} \\ &= \frac{dc}{l\lambda} \approx 19MHz \end{aligned} \tag{44}$$

Where $\nu$ is the laser frequency and $c$ is the speed of light. This is about 2.5 times the linewidth and it is comparable to what we observed in Figure 32(c).

## 5.3 clover beam shape

During my experiments of the new membrane, one of the key finding is this curious mode shape of the output laser beam. Among many other groups that have used similar high reflectivity photonic crystal structures, no such phenomenon was observed. [8][33] Thus we invested some time to seek our explanations for

the phenomenon. In this chapter, I will provide a detailed experimental observation of the phenomenon.

### 5.3.1 Earlier Observations with broad waist

A much weaker version of this phenomenon is first noticed on membrane 11 when I used a much wider beam waist at about 72$\mu$m. Even though the better quality of this membrane contributes to the effect, similar mode shape are observed on earlier membranes also Figure 34. This indicate that the phenomenon might be universal for this kind of membrane instead of from bad nano-fabrications.

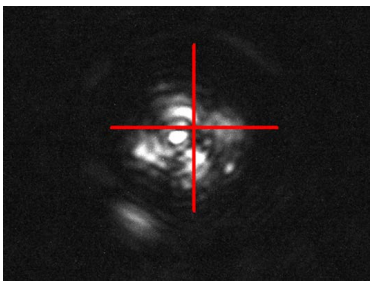

Figure 34: Old mode shape at 833.15nm. This mode has a diameter of about 70$\mu$m. The red cross in the middle represent the normal direction of the membrane shown in Figure 35. We can see a clover shape which hold an certain angle to the red cross.

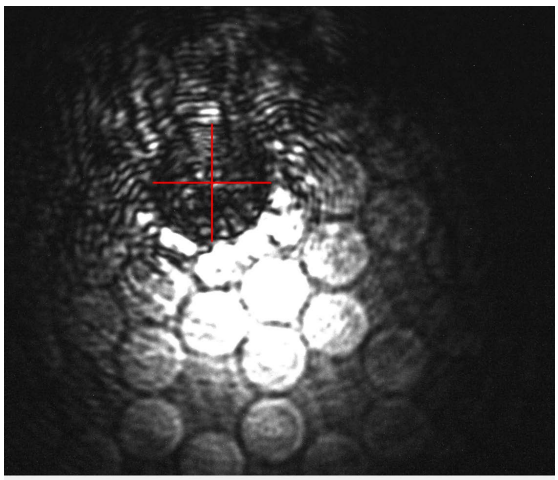

Figure 35: The red cross serves as a location and size mark of the photonic crystal(dark circle in the captured image). And the orientation of the cross is roughly aligned with the axis of symmetry of membrane phononic structures.

This shape here doesn't look very Gaussian-like. However, if we tune the wavelength away from our "center frequency", the foundamental mode shape will

become more and more Gaussian as the transmission of membrane increases. See Figure 36.

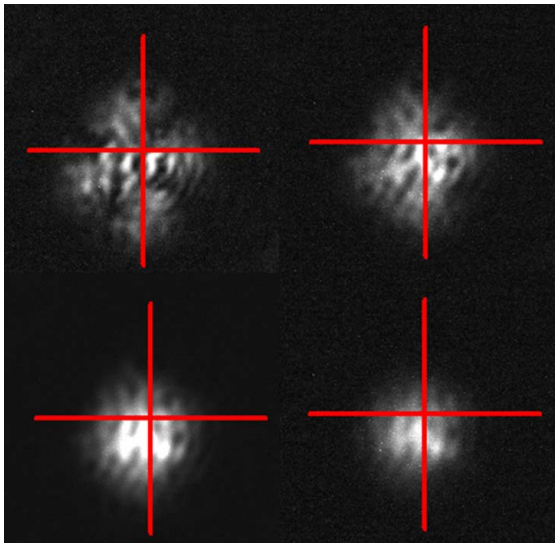

Figure 36: The mode shape looks more and more Gaussian as we tune the laser wavelength away from 833.15nm the "center frequency". They are acquired at wavelength: Top left: 833.15nm; Top right: 832.65nm; Bottom left: 832.15nm; Bottom right: 831.65nm.

This of course, was my verification of the peak is in fact the fundamental mode, instead of some higher order modes. However, when we narrowed down the beam waist to about 37$\mu$m, this clover phenomenon became more and more obvious. As shown in Figure 37. Here, no clover shape was observed for the reflection side, this implies that this clover shape is probably photonic lattice related and it only happens when light is transmitted through the photonic crystal.

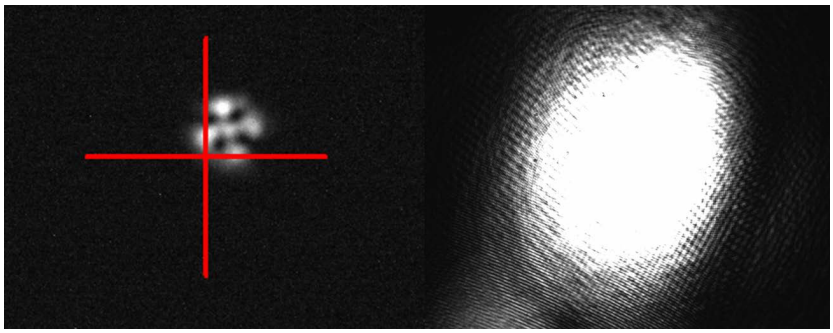

Figure 37: The fundamental mode(left) looks like a clover when we have 37$\mu$m beam waist. The plot on the right is the reflection mode shape for the same waist, but no clover shape observed.

It is also worth noticing that the orientation of this clover shape seems to be independent of beam size. In another word, the four 'petals' are always pointing at the same direction regardless of the beam size.

### 5.3.2 Investigation and Arguments

This finding leads to my curiosities of its origin.

My assumptions were:

1. It was from concave mirror defects, bad coatings or asymmetry.
2. It was from some membrane defects.
3. It was from PhC holes orientations.

Following these assumptions, I was expecting for some clues after related experiments. But sadly none of them provided me with much useful information.

**Frequency Tuning** As a verification of it being the fundamental mode, I ran some test on different frequencies and observed similar gaussian-approaching effects as shown in **??**. Despite the fact it approached gaussian when far from center frequency as expected, the mode shape also changed when I tuned the wavelengths.

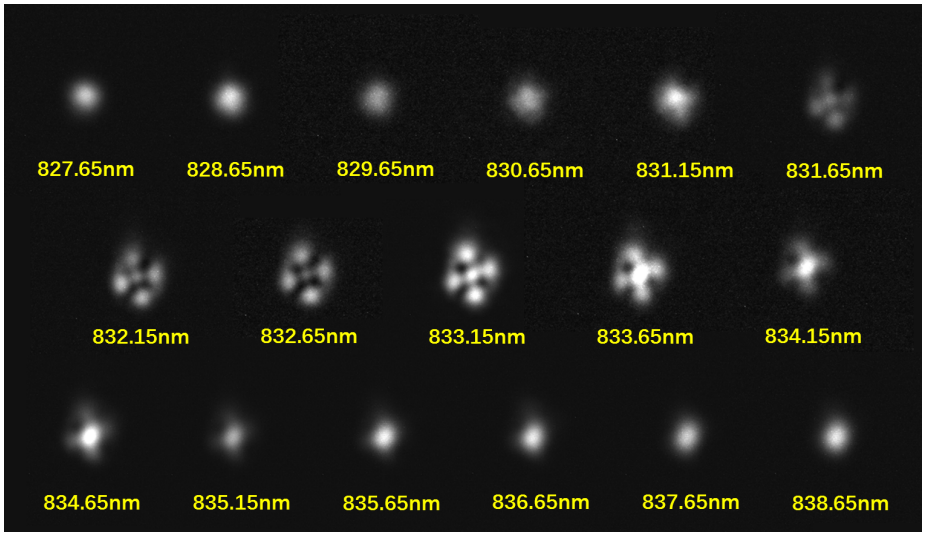


Figure 38: Clover shapes of transmission through the cavity at different wavelengths between 827.65nm and 838.65nm around the peak reflectivity at 833.15nm. The mode shape was captured by the camera 50cm behind the cavity as shown in plot We can observe a smooth transformation from a gaussian to clover shape and back to a gaussian. Another interesting fact is that this transition is asymmetric: for exmaple 832.15nm shape is very different from 834.15nm shape.

**Assumption 1: Rotating the mirror** The concave mirror was rotated multiple times when I was adjusting the cavity length, but the orientations of petals

remains the same. If it were a mirror related issue, we could have seen a rotation( or even change) of mode shape. Thus, this assumption can be excluded.

**Assumption 2: Cruising on the membrane** If this was a result of certain defects on the membrane, a change of mode position on membrane should lead to a significant change of mode shape. However, as we can see in Figure 39 this is not the case.

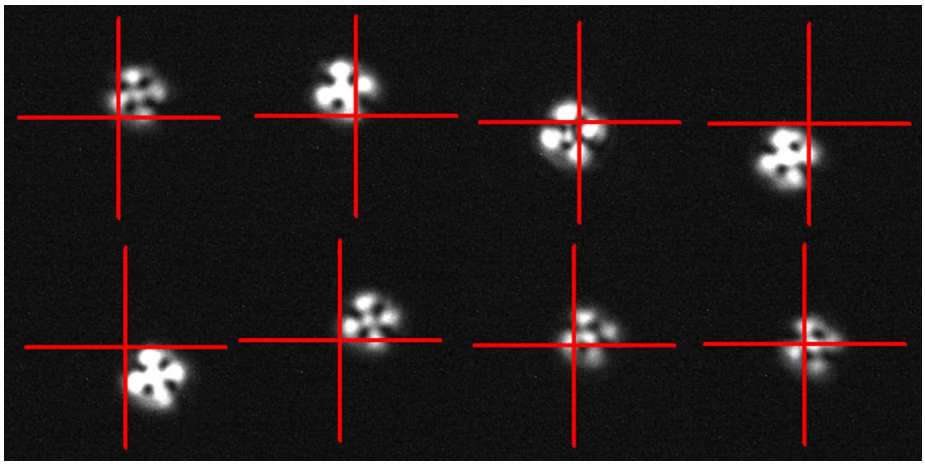

Figure 39: The mode shape remained roughly the same on different positions on the membrane. As before, the red cross here indicate the position of our photonic crystal, and the center of the cross is roughly the center of the PhC.

This is a good evidence against assumption 2, and indicates that the mode shape is not very dependent of its position on the membrane.

**Assumption 3: Flipping the membrane** Let us first assume the clover shape is related with the membrane fabrication direction(or the arrays of "photonic holes"). Then after we flip the membrane and using the other side for reflection, we should expect an mirrored image of this clover shape as shown in **??**.

The other issue is the clamping orientation. Luckily, our clamping orientation of membrane can only be changed by 90 degrees, same as the axis of the clover shape and the axis of photonic hole arrays. So even if the shape is related to photonic structures, it is independent of our clamping. More precisely, even if I rotate the membrane by 90 degrees during my flipping, I won't make a difference to the clover shape. Thus, under the condition that assumption 3 is real, the top petal should point at top right direction after my flipping. However, as we see in **??**, the flipping of the membrane did nothing to the mode shape.

But we should remember that, this statement is only true if the flipping axis

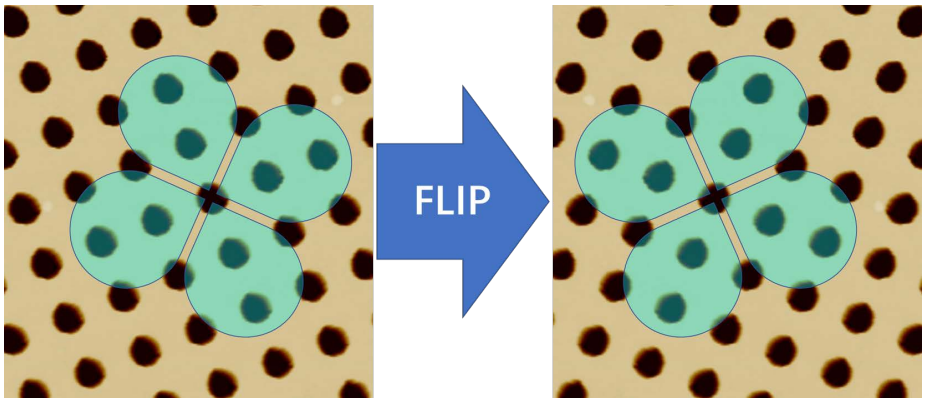


Figure 40: If the assumption were true, then we should expect a mirrored beam shape.

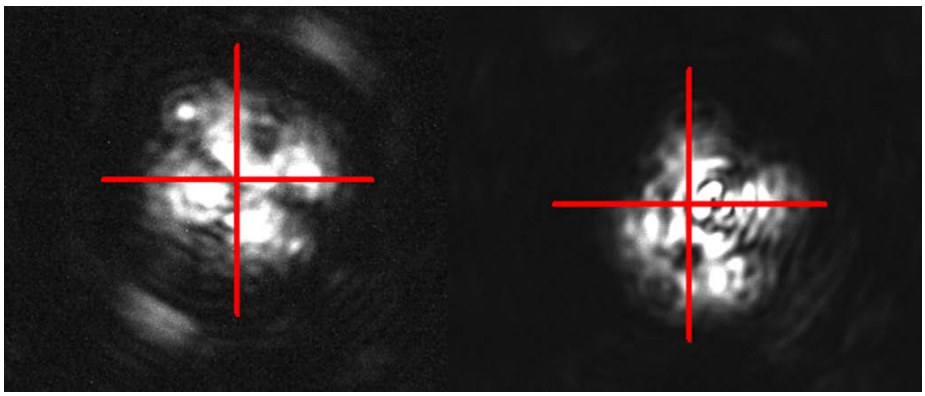

Figure 41: The mode shape remained the same after I flipped the membrane. From left to right are images before and after the flipping.

is not one of the axis of clover symmetry. It turned out to be not as trivial as it sounded to verify because it is not easy to relate the flipping axis and the clover orientation on the camera, due to the symmetric shape of the phononic patterns. Thus, we need to draw the following deductions and experiment.

### 5.3.3 Verification of flipping axis

A neat verification of the flipping axis is needed in order to determine the relations between the flipping axis and the clover beam shape. In our microscopic regime, we can only determine the flipping axis directly from the axis of symmetry for the square membrane. We can deduce the photonic structure orientation is aligned with the flipping axis of the membrane from the design diagram of the membrane. But since the phononic structures we observed on the camera has 12 axis of symmetry, we still need to struggle our way to pick the real ones.

The first method we tried was to use a string that aligned with flipping axis. However, due to the extremely blurry image on the camera(the focus of the camera is at the membrane plane), this method is no longer an option.

We eventually come up with the knife edge clipping method to complete the job. We do this by slowly moving a knife edge that parallel to the symmetric axis to clip the beam just beneath the cavity. Since in principle, the clipping of a knife-edge with the beam can create a very clear diffraction pattern that is perpendicular to the knife edge as shown in Figure 42. We are now able to determine both flipping axis of the membrane(green lines in the plot), which are also the two square lattice orientations. Now we are able to tell from the plot that the green axis is also the axis of symmetry for our clover shape at the corner. The green axis has an angle of 32 degrees to the red

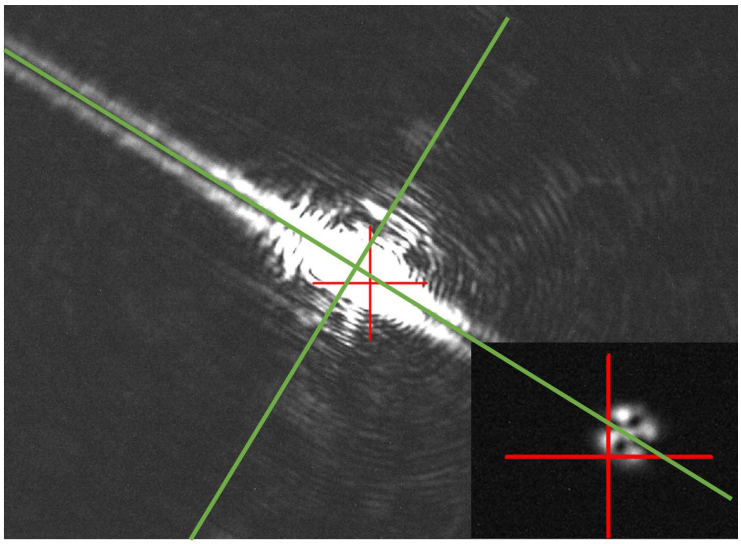

Figure 42: The knife-edge diffraction pattern(main figure) and the clover shape before clipping(bottom right). The red cross in the image serves as a indicator for the normal orientation of the camera, the green lines are guidelines drawn from the diffraction pattern that is parallel to the square lattice orientations. We can see from the clover figure that the green line is also its axis of symmetry.

However, even now we verified this phenomenon is possibly related to the photonic structures, it is still not quite clear about the physics behind it.

Apart from our verification of clover shape on the camera which could be merely an image on the camera but doesn't reflect anything on the membrane, I verified the clover shape beam can remain stable for a relatively long distance, as shown in Figure 43. I can still see a quite clean shape at roughly a meter after the light leaving the cavity. This serves as a side information of this phenomenon to exclude the possibility this shape was because of some camera issues. And by using the membrane we successfully created a physical clover shape beam.

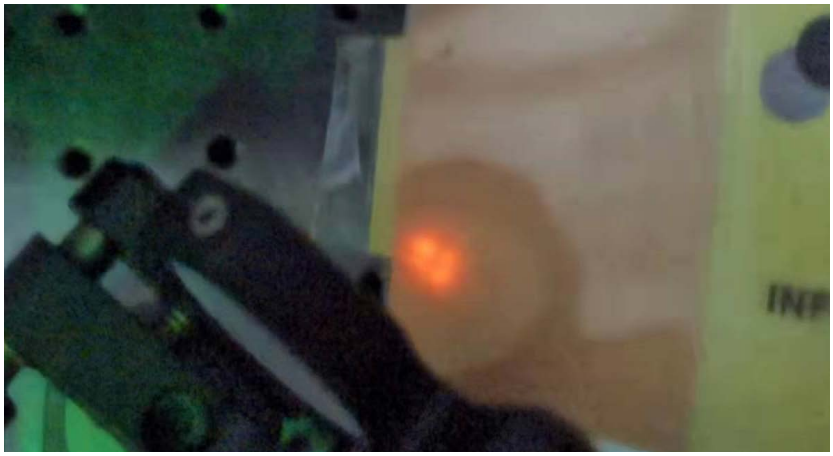

Figure 43: The mode shape can remain as the beam shape after leaving the cavity for about 200mm. Here the beam waist on the membrane is $2w_0 = 37\mu m$.

### 5.3.4 Higher order modes

I observed some higher order modes on the spectrum when the alignment wasn't perfect at the wavelength 833.15nm (centre). The shape is shown in Figure 44. Even though some of them seems quite similar comparing to the common Gaussian higher order modes [14] but others are not.

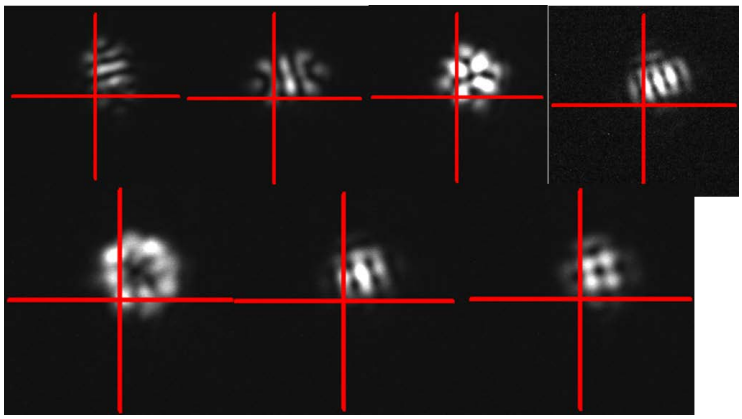

Figure 44: Higher order modes of clover shape mode.

### 5.3.5 Mode-waist relationship

From our discussions above, we are able to see that there is a waist-clover relation here, and the clover shape becomes sharper at small waist. The mode shape-waist relationship is demonstrated in Figure 45.

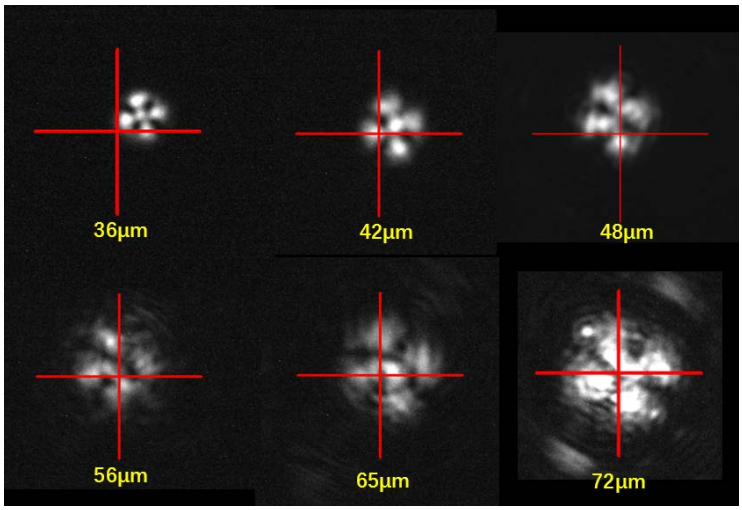


Figure 45: The shape-waist relationship. When our beam waist varies from 36 $\mu$m to 72 $\mu$m, the clover beam shape become more and more blurry.

Thus, we are now able to tell from our former discussion that we have this curious phenomenon that haven't been observed before. We will see a whole new chapter for simulation investigation on this problem in section 7.

# 6 Methods for result analysis

During my months of photonic crystal membrane characterizations, I tried and developed many different methods to calculate the transmission and scattering loss of my concave mirror photonic crystal cavity. Due to the high scattering loss nature and potential light path coupling issue of the photonic crystal membrane, many of the common method cannot determine the scattering loss accurately.

Thus, in this chapter we compare three main methods we tried to acquire the scattering loss result and compare their final errors and accuracy of results. All these methods can be useful for certain membrane parameters, but not all. In this chapter I will provide an overall comparison for all the methods.

## 6.1 R-T measurements

The most straight forward way of processing the data is the common R-T method. This method has been used to characterize the scattering loss of cavity mirrors in multiple cases 20 years ago at Caltech and JILA[34]. In the method they proposed, there are two limitations: first their method requires knowledge of the transmittivity of two mirrors in advance; and second their measurements require high finesse (480,000 as they mentioned in the article) to produce a precise result. Thus, we made some modifications of their approach on the effort of providing a more universal approach that can separate different loss elements from each other.

Different from what JILA group did before that they measured the mirror transmission independently from direct measurements using powermeter, we were trying to develop a method that can determine all unknown variables at the same time using a single cavity and three photo-diode detectors. The reason we started another approach is because we want to always keep the concave mirror as a crosscheck to make sure that there will not be some systematic errors on the optical path that can keep me from getting the real measurements.

### 6.1.1 results and uncertainty

The result using the standard method was never truly used because of the

### 6.1.2 Introductions to group analysis

When using this method, we are actually using it under some basic assumptions that I made. But before we talk about the assumptions in details, please allow me to first use an example to provide a clear picture about why we need two groups of data at two neighbour frequencies.

As a example, if we want to solve the value for $t_1^2$ using reflectivity test results and Equation 8, we could never get only one value because of the symmetric

feature of cavity. This is demonstrated in Equation 45. Even under the same $\gamma$ and R, T conditions, we will still get two solutions from the . This is why we always need another group of data to exclude one solution. It is even more obvious if we try to solve Equation 8, and reorganize it like this:

$$t_1^2 = \frac{(1 \pm \sqrt{R})\gamma}{2} \tag{45}$$

Thus, we always need at least two group of data to determine the sign in this equation. And then, we can insert what we got from Equation 45 to the following equation reorganized from Equation 4 to get the value of $t_2^2$:

$$t_2^2 = \frac{T\gamma^2}{4t_1^2} \tag{46}$$

But here we actually made two important assumptions:

1, the scattering loss $\gamma$ is independent of laser frequencies in 1nm range.
2, the transmission coefficient $t_1$ is also independent of laser frequencies in 1nm range.

These assumptions seems to be valid from our test result if we keep our laser wavelength within a limited range around 833nm.

### 6.1.3 Analysis

After we finish all our measurements, we can summarize what we have in our hands right now, and use a new group of data at 833.65nm acquired by the same method:

| Wavelength | R | T | $\gamma$ |
|---|---|---|---|
| 833.155nm | 0.48 | 0.285 | 0.00276 |
| 832.75nm | 0.39 | 0.155 | 0.00243 |
| 833.65nm | 0.65 | 0.260 | 0.00477 |

After we apply Equation 4 and Equation 8 to first group of data, we can solve and get the result from wavelength 833.155nm:

| Result 833.155nm | $t_1^2$ | $t_2^2$ | Scattering Loss |
|---|---|---|---|
| 1 | 0.00234 | 0.00023 | 0.00019 |
| 2 | 0.00042 | 0.00129 | 0.00105 |

The two groups of result above can to narrowed down to one if we introduced our second group of data:

| Result 832.75nm | $t_1^2$ | $t_2^2$ | Scattering Loss |
|---|---|---|---|
| 1 | 0.00197 | 0.00028 | 0.00018 |
| 2 | 0.00046 | 0.00050 | 0.00147 |

But here we noticed that it is not easy for us to determine now. This is because these two groups of data are quite close to each other. This is why we introduce the third group of data at 833.65nm at the beginning of this section:

| Result 833.65nm | $t_1^2$ | $t_2^2$ | Scattering Loss |
|---|---|---|---|
| 1 | 0.00439 | 0.00034 | 0.00004 |
| 2 | 0.00046 | 0.00313 | 0.00117 |

From our assumptions at 6.1.2, we should expect a similar scattering loss and $t_1^2$ for all groups of data. Thus we know that only the second data in each group is possible.

We can also introduce any other group of results as verifications:

For example at 832.55nm, we have $R = 0.42, T = 0.225, \gamma = 0.00275$. The result for the group of measurement is:

| Result 832.55nm | $t_1^2$ | $t_2^2$ | Scattering Loss |
|---|---|---|---|
| 1 | 0.00227 | 0.00019 | 0.00029 |
| 2 | 0.00048 | 0.0089 | 0.00138 |

From all these data we can tell that even though it seems that we can exclude one of the result in each group, the variation for the final scattering loss is still pretty big. Thus, we should do a error analysis to see if these results are inside the error bar or not. Further investigation of errors will be introduced in 6.1.5.

### 6.1.4 Result explanations

As a side explanations for where the about 1300ppm errors could have come from, we can take a look at this strange beam shape in Figure 46:

This finding actually consist with what we found when looking at the photonic crystal under the microscope using 50x lens in Figure 9.

### 6.1.5 Error analysis and the limitation of group analysis

For the error of finesse, we can use repeated measurements to learn about the standard deviation of measurement, and then we will have some idea about the accuracy of finesse measurement. Accuracy of finesse: $\pm 1\%$.

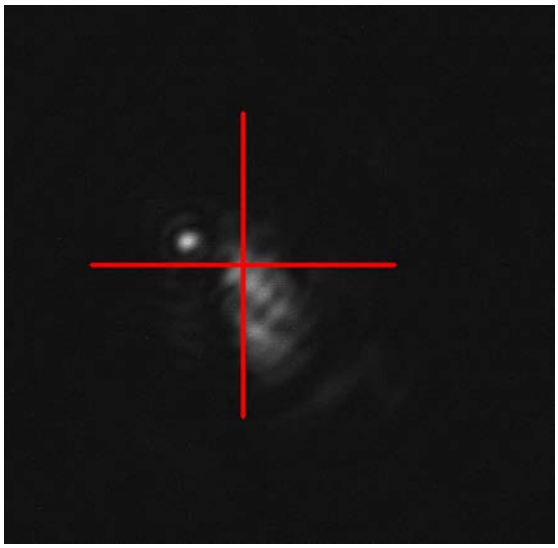

Figure 46: Beam shape of the cavity transmission close to resonance. At the left top part of the defect, there is a bright spot, which indicates that there is some leakage of light over there.

As for reflectivity and transmittivity, since they might have some systematic errors(due to imperfect coupling into the fundamental mode), repeat measurements won't give us answer to these sort of errors. Since the spectrum was quite clean for the data we use here, and calibration for R is hard to be far from its true value, we will assign R and T with $\pm 5\%$ and $\pm 8\%$ of error respectively. The two measurement uncertainty here came from the data noise we acquired on the photodiode detector as we demonstrated in Figure 25 and Figure 22.

Thus, we can use error propagation method to get the error for each of our measurements:

| | $\gamma$ | $t_1^2$ | $t_2^2$ | Scattering Loss |
|---|---|---|---|---|
| Result | 0.00243 | 0.00046 | 0.00050 | 0.00147 |
| Error | 0.00002 | 0.00003 | 0.00006 | 0.00007 |

We can see that even though the value of $t_1^2$ are all within the error bar(we used an input mirror with the labelled transmission $t_1^2 = 500pm$), scattering loss is hardly acceptable. The lowest scattering loss is 0.00105 at 833.155nm, which is more than $3\sigma$ away from the scattering loss at 832.75nm

We should either accept that the scattering loss is quite dependent on color, the errors we made in experiment is way bigger than we expected, or there is some other systematic error not included.

Here I think the third one is more possible at this stage.

## 6.2 Mode matching modelling

It is hard to quantify how bad we matched the mode, so it is reasonable to investigate the situation that we had a bad mode matching. If we succeed, we can spend less time finding perfect mode matching and simply use our method to do a compensation to get the theoretical T and R value from our imperfect data.

### 6.2.1 Mode coupling theory

To calibrate the mode matching, we simply add an input coupling coefficient to our old theory:

In our situation, we can assume that our target mode only gets a certain proportion of the total power, which is the mode coupling coefficient $A$. In this case, the peaks we saw from experiment is $A$ times its value if we had 100% coupling into the fundamental mode. For convenience, we say that the inverse of $A$ is $\alpha$. The value of $\alpha$ is the inverse of input fundamental mode coupling coefficient, which means how many times we could "enlarge" the dips or peaks (perfect coupling) by ignoring the other modes. I find this a better way to use in calculation because it provides a more intuitive and cleaner way of our expression.

Thus, we can say that the actual transmission and reflection of the fundamental mode is(if we had 100% coupling into it):

$$\begin{aligned} R_{fm} &= 1 - \alpha(1 - R) \\ &= 1 - \alpha + \alpha R \end{aligned} \tag{47}$$

$$T_{fm} = \alpha T \tag{48}$$

If we assume the mode matching quality (when we do not move the concave mirror) is very similar at the target frequency range ($\pm$1nm), we can use different groups of measurements at different frequencies to determine the mode matching percentage.

If we insert Equation 4 and Equation 9 into Equation 74 and Equation 48, we will have the full expression for transmission and reflection when we have two groups of data at different frequencies:

$$R_{f1} = 1 - \alpha + \alpha(1 - \frac{2t_1^2}{\gamma_{f1}})^2 \tag{49}$$

$$R_{f2} = 1 - \alpha + \alpha(1 - \frac{2t_1^2}{\gamma_{f2}})^2 \tag{50}$$

$$T_{f1} = \alpha \frac{4t_1^2 t_{2f1}^2}{\gamma_{f1}^2} \tag{51}$$

$$T_{f2} = \alpha \frac{4t_1^2 t_{2f2}^2}{\gamma_{f2}^2} \tag{52}$$

Here f1 and f2 correspond to the first frequency and second frequency we acquired from measurements respectively. There are four unknown variables in these equations: $\alpha, t_1^2, t_{2f1}^2, t_{2f2}^2$. Thus, the equation set should be solvable here.

The total assumptions we implied here are:
1, the scattering loss $\gamma$ is independent of laser frequencies in 1nm range.
2, the transmission coefficient $t_1$ is also independent of laser frequencies in 1nm range.
3, the mode matching coefficient $\alpha$ is independent of laser color.

### 6.2.2 New analysis

Now we can apply the mode matching theory into our calculations. This is getting more and more complicated so we simply put our two groups of data below (see 6.1.3) into the calculator to solve the equation. I used Wolfram Alpha.

| Wavelength | R | T | $\gamma$ |
|---|---|---|---|
| 833.155nm | 0.48 | 0.285 | 0.00276 |
| 832.75nm | 0.39 | 0.155 | 0.00243 |
| 832.55nm | 0.42 | 0.225 | 0.00275 |
| 833.65nm | 0.65 | 0.260 | 0.00477 |

After we put these data into the calculator by using Equation 49 and Equation 50, the result is not very pleasant. The result we had for all combinations are in Figure 47.

We can clearly see from the results that this method is unreliable, because first our results are very divergent from each other, and second most of them are not even possible. This is because if we remember in 6.2.1, by definition, the value of mode matching coefficient 'A' is the inverse value of $\alpha$. Since the coefficient must have a value between 0 and 1, the value of $\alpha$ must be bigger than one and positive. Thus, from the result our modelling or calculation is unsuccessful for some reason.

Here I guessed what happened here is that the value of alpha is way to sensitive to the value of R and $\gamma$. But we should be able to verify this by doing the

error propagation. If the result is sensitive to some certain variables, we should expect a huge uncertainty for the value of $\alpha$ or $t_1^2$.

### 6.2.3 Mode matching error analysis

Since the complexity here increased a lot, we need to find some smarter way to analyze the errors. I tried the most common (but also most tedious) way to get the error, but also invested a bit more time into some other method for sensitivity analysis. But the other methods didn't seem to be awarding yet.

**Equation solving and error propagation** Here I first use a "brutal" way to get the result. I used a method similar as Equation 45 to acquire an expression for $t_1^2$ using $\alpha$ as a variable. Here is the result I finally got:

$$t_1^2 = \frac{\gamma\alpha \pm \sqrt{\gamma^2\alpha(R+\alpha-1)}}{2\alpha} \tag{53}$$

But sadly this is still not able to do any error propagation yet. But if we make two sets of data at different frequencies and use Equation 49 and Equation 50 get a common expression for $t_1^2$. We can surprisingly simplify the equation by a lot. We will get a equation as below:(for simplicity of expression, only in this section we use $R_1, \gamma_1, R_2, \gamma_2$ to replace $R_{f1}, \gamma_{f1}, R_{f2}, \gamma_{f2}$, and T for $t_1^2$)

$$R_1 - 1 = \frac{4\alpha T(T-\gamma_1)}{\gamma_1^2} \tag{54}$$

$$R_2 - 1 = \frac{4\alpha T(T-\gamma_2)}{\gamma_2^2} \tag{55}$$

Thus, we can see that if we divide Equation 54 by Equation 55, we can remove the $\alpha$ from it. Then we will have:

$$\frac{R_1-1}{R_2-1} = \frac{\gamma_2^2(T-\gamma_1)}{\gamma_1^2(T-\gamma_2)} \tag{56}$$

After we reorganized the equation, we can get a expression for T as:

$$T = \frac{\gamma_1\gamma_2[\gamma_1(R_1-1) - \gamma_2(R_2-1)]}{\gamma_1^2(R_1-1) - \gamma_2^2(R_2-1)} \tag{57}$$

Thus, we can use the error propagation method to get the propagation expression of it(with four variables):

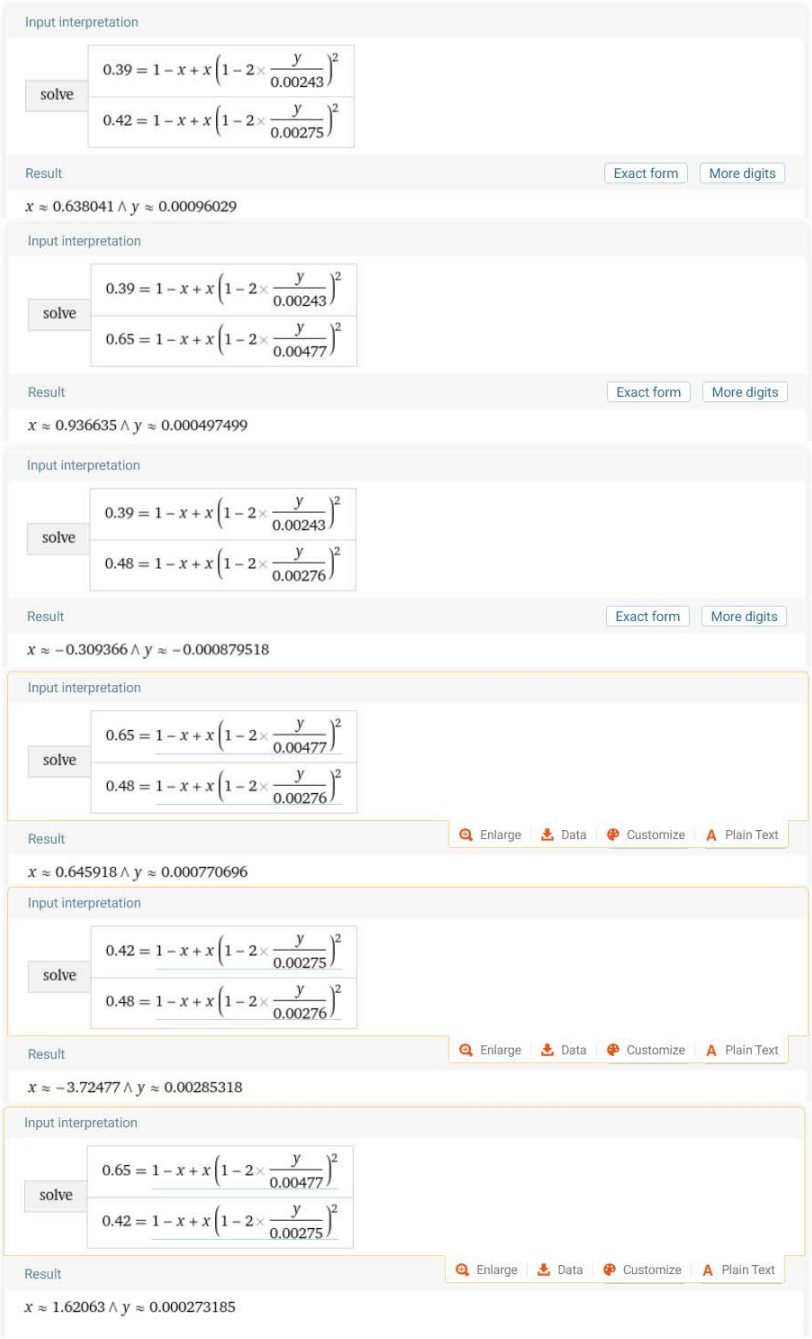


Figure 47: Results calculated by Wolfram Alpha, website at https://www.wolframalpha.com. Here x and y stand for $\alpha$ and $t_1^2$ in this article. We can clearly see that our results are very divergent from each other and most of them are not even possible.

$$\sigma T = \sqrt{\frac{\begin{array}{r}\gamma_1^4\gamma_2^2\sigma_{R1}^2\left(-\gamma_1^2\left(R_1-1\right)+\gamma_1\left(\gamma_1\left(R_1-1\right)-\gamma_2\left(R_2-1\right)\right)+\gamma_2^2\left(R_2-1\right)\right)^2 \\ +\gamma_1^2\gamma_2^4\sigma_{R2}^2\left(-\gamma_1^2\left(R_1-1\right)+\gamma_2^2\left(R_2-1\right)+\gamma_2\left(\gamma_1\left(R_1-1\right)-\gamma_2\left(R_2-1\right)\right)\right)^2 \\ +\gamma_1^2\sigma_{\gamma 2}^2\left(2\gamma_2^2\left(R_2-1\right)\left(\gamma_1\left(R_1-1\right)-\gamma_2\left(R_2-1\right)\right)+\left(\gamma_1\left(R_1-1\right)-2\gamma_2\left(R_2-1\right)\right)...\right)^2 \\ +\gamma_2^2\sigma_{\gamma 1}^2\left(-2\gamma_1^2\left(R_1-1\right)\left(\gamma_1\left(R_1-1\right)-\gamma_2\left(R_2-1\right)\right)+...\right)^2\end{array}}{\left(\gamma_1^2\left(R_1-1\right)-\gamma_2^2\left(R_2-1\right)\right)^4}} \tag{58}$$

From the equation above we can get our result from each pair of measurements shown in Figure 47. All the results are collected in this table:

| | 1 | 2 | 3 | 4 | 5 | 6 |
|---|---|---|---|---|---|---|
| $t_1^2$ Result | 0.00096 | 0.00050 | -0.00087 | 0.00077 | 0.00285 | 0.00027 |
| Error | 0.00040 | 0.00033 | 0.00199 | 0.00041 | 0.00045 | 0.00052 |

From the results above, we can conclude that it is not wise for us to consider this mode as a trustworthy one. The errors here can hardly provide us with any useful information. But the fifth data still doesn't consist with the others or the 500ppm value from the mirror measurements. This could indicate that our method to calculate the sensitivity of variables still has some flaws.

**Limitation of method** From 6.2.3 we can see that as soon as we include the mode matching coefficient into the model, the uncertainty of the $t_1^2$ measurement suddenly explodes. We might be able to find a better way to introduce this coefficient, so that it will not flood the existed variable with extra uncertainties. But the question is if it is worth the effort.

The reason I wanted to include this coefficient in the first place is to safe the time and effort on mode matching, but now it turned out to be more time consuming.

But if I am going to spend more time on this topic, I will use another group of data from the 1000ppm mirror to convince myself on the topic. And I think if I can get a accurate measurement on the $t_1^2$ directly, that will also open a window for us to reuse this method. Because in this case, we can measure the value of $\alpha$ directly. After that, the final uncertainty of $\alpha$ can possibly be limited within $\pm 3\%$.

## 6.3 Pairing method

After we realize that we could not achieve enough sensitivity of scattering loss measurements at our center frequencies, and the coupling rate of our measurements could lead to much more tricky situation, we developed the pairing method which eventually finalize our seeking of different measurement methods.

### 6.3.1 Method and calculations

The basic idea of pairing method is to use a tune-able laser to measure different round trip losses at different wavelengths within a short range(1nm). However, this method is also based on two approximations:
1, Scattering loss is independent of wavelength in a small range.
2, The mirror(concave one on the top in our case) transmittivity remains unchanged when we tune the laser in a certain range.

After these two conditions full-filled, we are able to use multiple pairs of round-trip loss and transmission measurements made at different wavelength to acquire the following equations:

$$\gamma_{f1} - \gamma_{f2} = t_{2f1} - t_{2f2} \tag{59}$$

Where $\gamma$ stands for the round-trip loss, $t_2$ is membrane transmission and $f_1$ $f_2$ indicate two different frequencies. Remember our former deduction about the cavity transmission expression Equation 4, we have:

$$T_{f1} = \frac{4t_1^2 t_{2f1}^2}{\gamma_{f1}^2} \tag{60}$$

$$T_{f2} = \frac{4t_1^2 t_{2f2}^2}{\gamma_{f2}^2} \tag{61}$$

From Equation 60 and Equation 61 and insert the relation shown in Equation 59, we can get the transmission expression as:

$$t_{2f2}^2 = \frac{T_{f2}\gamma_{f1}\gamma_{f2}^2 - T_{f2}\gamma_{f2}^3}{T_{f1}\gamma_{f2}^2 - T_{f2}\gamma_{f2}^2} \tag{62}$$

Using textbook error propagation method, the uncertainty of this transmission measurement has the expression of:

$$\sigma(t_{2f2}^2) = \sqrt{(\frac{\partial(t_{2f2}^2)}{\partial\gamma_{f1}}\Delta\gamma_{f1})^2 + (\frac{\partial(t_{2f2}^2)}{\partial\gamma_{f2}}\Delta\gamma_{f2})^2 + (\frac{\partial(t_{2f2}^2)}{\partial T_{f1}}\Delta T_{f1})^2 + (\frac{\partial(t_{2f2}^2)}{\partial T_{f2}}\Delta T_{f2})^2} \tag{63}$$

After we acquire one of the membrane transmission, we can now obtain the scattering loss $\beta$ by using Equation 62 and Equation 19:

$$\begin{aligned}\beta &= \gamma_{f2} - t_1^2 - t_{2f2}^2 \\ &= \gamma_{f2} - t_1^2 - \frac{T_{f2}\gamma_{f1}\gamma_{f2}^2 - T_{f2}\gamma_{f2}^3}{T_{f1}\gamma_{f2}^2 - T_{f2}\gamma_{f2}^2}\end{aligned} \tag{64}$$

Here we can use the error propagation again to obtain the error of the scattering loss we just obtained in Equation 64:

$$\sigma\beta = \sqrt{\begin{aligned}&(\tfrac{\partial\beta}{\partial\gamma_{f1}}\Delta\gamma_{f1})^2 + (\tfrac{\partial\beta}{\partial\gamma_{f2}}\Delta\gamma_{f2})^2 + (\tfrac{\partial\beta}{\partial T_{f1}}\Delta T_{f1})^2 \\ &\quad + (\tfrac{\partial\beta}{\partial T_{f2}}\Delta T_{f2})^2 + (\tfrac{\partial\beta}{\partial(t_1^2)}\Delta(t_1^2))^2\end{aligned}} \tag{65}$$

### 6.3.2 Results and advantages

A demonstration of results gained using pairing method is shown below, the following data is taken at the waist on membrane of $2w_0 = 65\mu m$. First we can acquire the round trip loss by finesse as we discussed in subsection 2.2 with 6 repeats. We do this at different frequencies(at least 4 to acquire 5-6 groups of usable pairs). We turn off the EOM and measure the relative transmission peak height after calibrations for each of the frequencies. We are now able to acquire the results similar as what we are showing below. Here we should keep in mind that we should keep the frequency range tight but also be able to distinguish from each other. This is an interesting trade-off we should take, because if we "mate" two frequencies that scattering losses or peaks are too similar to each other, we will have huge propagation errors when we are trying to subtract them. However, if they are too far from each other, we will be risking our neck that the frequency differences leading to too much systematic errors such as different mirror reflectivities or even different scattering loss at different wavelengths. Thus, from our experience, the suitable range should be within 1 nm.

| **Wavelength/nm** | **Round trip loss /ppm** | **RTL errors /ppm** | **Peak height (no units)** | **Peak height errors** |
|---|---|---|---|---|
| 833.15 | 2244 | 21 | 412 | 10 |
| 833.00 | 2270 | 15 | 417 | 10 |
| 832.75 | 2776 | 15 | 679 | 15 |
| 832.55 | 3561 | 28 | 806 | 20 |

The next step is to get pairs, and make the calculation using Equation 62. Here a important knowlegde is how to pick pairs. We selected 5 pairs from this group of data, and they are shown in the table below. Here we pick pairs based on the sole principle to avoid round trip losses that are too close to each other(such as 833.15nm and 830.00nm pairs).

From the table, we are now able to determine our estimated scattering loss error is 780±20 ppm, and the minimum transmission at peak reflectivity is:

| Wave- length 1/nm | Wave- length 2/nm | Scattering loss /ppm | Errors /ppm |
|---|---|---|---|
| 833.15 | 832.75 | 750 | 40 |
| 833.15 | 832.55 | 770 | 40 |
| 833.00 | 832.75 | 790 | 40 |
| 833.00 | 832.55 | 780 | 40 |
| 832.75 | 832.55 | 810 | 60 |

320±20ppm. This scattering loss of this result is at around 2% level.

The results acquired using pairing method is demonstrated in Figure 27.

**Advantages of pairing method** The advantages for the pairing method is significant comparing to the other two methods.

First, the pairing method is insensitive to the in-coupling rate into the cavity. We acquired very similar result with relatively low coupling rate and high coupling rate. This advantages can save people a lot of time doing calibrations and alignment which could be very tedious and time consuming.

Second, the pairing method is in principle indifferent to the other form of losses on the optical path, since it will cancel out all the loss that is proportional to its power. Thus, with pairing method, we do not need the optical path calibration required by other methods.

Third advantage is that the pairing method requires no reflection arm detection. The reflection detection is not only tedious to align, but can also cause many systematic errors in many of the setups. One of the most common systematic error was from the reflection of the calibration arms in our setup as shown in Figure 30. The reflected power from the calibration photo-diode detector(PD) can sometimes enter the reflection arm that cause some quite significant errors. This of course can be avoided by turning the calibration PD to an angle. However, since the calibration PD is near the focal point of the lens, tuning is still not easy to aviod this phenomenon. Thus, the pairing method saved us from the efforts of changing too much in the optical path.

The final advantage is of course its accuracy when the loss/transmission ratio is high enough. In pinciple, we can do many different pairs of measurement and acquire very high precision (2-3% error for 6 repeats of measurements at relatively big waist).

**Limitations of pairing method** Even though the pairing method provide us with nice results at large beam waists. Its limitations are still quite obvious. If we use narrow beam waists for our results where scattering loss/ transmission ratio is very high, we could end up with some huge errors due to the fact

that the peak heights on resonance can be very similar within 1nm range. But this is a limitation for most methods since none of them are able to separate a small scattering loss from huge membrane transmission loss. The second limitation is due to the change of clover shape at different frequencies. For most of our experiment, we will focus our light on photo-diode detectors but also not too much for a common gaussian beam as for the detector has a area of about 1mm×1mm size. It would be fine for the general cases but when the mode shape can magically grow to a much bigger clover beam, this would lead to calibration errors that are really harmful to the results. But this limitation can be avoided by moving the photodiode detector closer to the focal point and by using a lens with smaller focal length.

## 6.4 Comparison of methods

After we demonstrated how we obtain results with three(or four) different methods, now we should put them together to make our comparison, here $\phi$ = scattering loss/transmission loss:

| Method | Standard R-T | Group measure-ments | Mode matching | Pairing method |
|---|---|---|---|---|
| **Requirement for measurement of mirror** | **Yes** | **No** | **No** | **Yes** |
| **Scattering loss accuracy for high $\phi$ (experimental case)** | **Moderate** | **Moderate** | **Low** | **Very high** |
| **Scattering loss accuracy for low $\phi$ (desired case)** | **Moderate** | **Moderate** | **Moderate** | **Moderate** |
| **Is cavity coupling rate accounted** | **No** | **No** | **Yes** | **Yes** |
| **Is other optical loss on light path compensated** | **No** | **No** | **No** | **Yes** |
| **Difficulty for alignments** | **High** | **High** | **Low** | **Low** |
| **Difficulty to obtain results** | **Moderate** | **High** | **High** | **High** |
| **Is reflection signal needed** | **Yes** | **Yes** | **Yes** | **No** |
| **Is transmission calibration needed** | **Yes** | **Yes** | **Yes** | **No** |

Table 4: Table for the comparison of different measurement methods that we used and their sensitivity/benefits comparison.

From Table 4, we can see that pairing method is superior in terms of accuracy for the high scattering loss/transmission loss ratio for the membrane we have at hand, and it is the least alignment time-consuming method. For our case, since we wanted to test different membranes with different cavity length and different concave mirrors, heavy alignments could be way too inefficient. But if we have a low scattering loss PhC membrane in the future, the standard R-T method can still be useful and worth the time invested for the alignment.

# 7 Simulations of clover shape

Following our discussion in subsection 5.3, we realized that this new phenomenon is possibly related to the photonic structures. Photonic structures had been found influencial on mode shapes about intensity distribution and observed interference of the beam generated by the metasurface [35].

Keeping this suspicion in mind, in this section we want to study the origin of the clover shape by simulations, since the clover shape could turn out to be deadly for our multi-cavity coupling rate since we are not yet sure if the intracavity mode is Gaussian or not with the clover as an far field output.

In this section, I worked with helping hands from simulation experts Anders Simonsen and Georg Enzian. We eventually found a way to combine COMSOL simulation and Fox-Li simulation approach[36][37] to provide a satisfying explanation for the clover shape mode and cavity transmission.

## 7.1 COMSOL simulation

COMSOL multiphysics is a powerful tool for the simulation of electromagnetic waves using finite element method(FEM). It has been used intensively for photonic structure numerical simulations in the last ten years [38] [39]. Even though the COMSOL multiphysics has been proved powerful for maxwell equation wave optics, it has a limitation for our simulation, which is it is very hard to simulate a limited region photonic slab($200\mu m \times 200\mu m$ for the photonic defect we used). This was due to the limited RAM we have for a common laptop or accessible computer.

Thus, in this section we will simulate the photonic structures as an infinite PhC crystal, and we will decompose our cavity mode into different plane waves in k-space[40]. By doing this, we can easily finish the COMSOL simulation in a reasonable time as plane wave incidence on infinite periods photonic crystal, while still being able to gain enough information for future Fox-Li method.

### 7.1.1 COMSOL setups

In this section we will describe simulations done for a Photonic Crystal (PhC). The simulations are for infinite-size membranes and are done with pure plane wave illumination while scanning both incident angle and azimuth angle. The COMSOL simulation method here has been developed and used before in other research center[41][42] as well as in Niels Bohr Institute[43], and I was also following the basic guidelines from COMSOL website[44] (Wave Optics Module User's Guide) to create a basic cell simulation.

The simulations are done in COMSOL Multiphysics 5.6 with use of the Wave Optics Module. S unit cell is designed as shown in Figure 48. The photonic

crystal simulation is a three dimensional design, where periodic boundary conditions have been used in x-y plane directions to create an infinite square lattice of holes. The lattice constant for the PhC is called a and the diameter of the holes are called d. The Port boundary conditions (in Electromagnetic Waves, Frequency Domain interface) is placed on the top and the bottom of the unit cells and are used to release the incident wave and to absorb the reflected and transmitted waves of order 0. The Diffraction Order are added to absorb outgoing waves of non-zero diffraction order. Here the index of refraction for $Si_3N_4$ is Re(n) = 1.9861 and Im(n) = $5 \times 10^6$ [45].

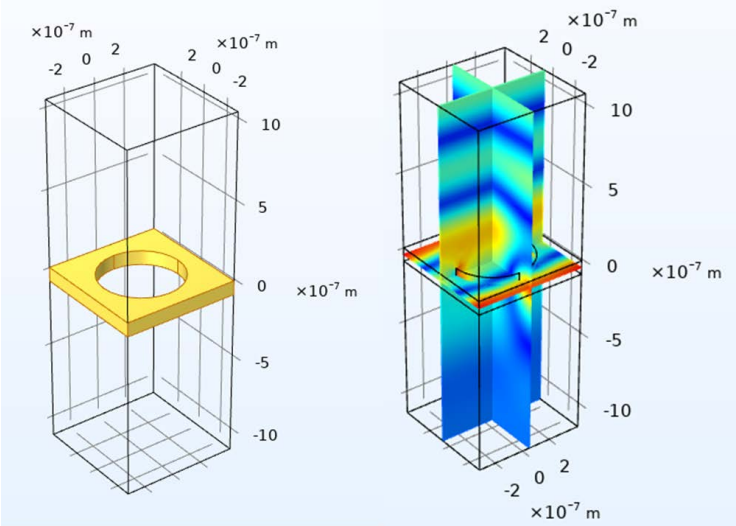


Figure 48: Geometry of one unit cell photonic crystal(left) and COMSOl plane wave simulation(right).

For our simulation above, we have various of data we can possibly use in simulation, those data are demonstrated in Table 5. Where the COMSOL parameters are real parameters measured under electron microscope by Dr.Anders Simonsen, while the 830.4nm peak reflectivity wavelength is determined in COMSOL using the measured results and scan over a range between 820nm till 850nm, with the result shown in Figure 49. The result indicate a small difference between the measured wavelength(833.15nm) and the simulated wavelength(830.4nm). This implies that either our measurement is not precise enough, or the fabrication imperfections are actually leading to some other effects. Even though the simulation result is not yet agreeing with experimental data, it still tells us a lot about what we discussed in Figure 6 about why our peak reflectivity is 20nm away from the designed parameters.

Now, we should move forward with the new 830.4nm simulation result instead of 833.15nm which is the experimental result. This is because in subsection 5.3 we conclude that the clover shape happened at peak reflectivity where the finesse is highest. Thus, we should use the simulated peak reflectivity 830.4nm to continue in order to get the results with the most obvious "clover shape",

| value type | designed parameters | real parameters | COMSOL parameters |
|---|---|---|---|
| thickness | 100nm | 88.5nm | 88.5nm |
| lattice constant | 734nm | 728nm | 728.3nm |
| lattice hole diameter | 511.2nm | 511nm | 511.2nm |
| Photonic crystal size | 200$\mu$m | 200$\mu$m | Unable to simulate |
| Peak wavelength | 852nm | 833nm | 830.4nm |

Table 5: Designed parameters and real parameters of photonic structures. We can see a very clear difference here. The real parameters here is measured by Dr. Anders Simonsen under electron microscope. The COMSOL parameter in the third column is a even more precise measurement under electron microscope, and the peak reflectivity wavelength is determined using the measured results.

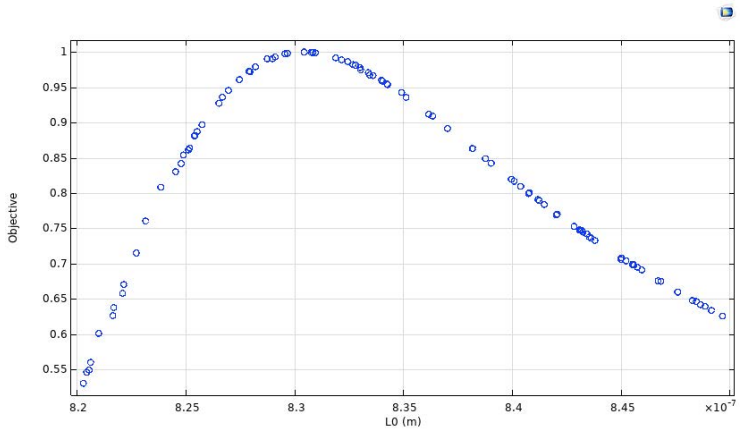


Figure 49: COMSOL simulation of scanning wavelength in order to find the peak reflectivity of the photonic crystal. We acquired the peak reflectivity at 830.4nm from the simulation result.

which is the priority of our simulation.

With all the parameters set, we should now acquire the plane wave parameters we need as decomposition of Gaussian cavity mode. Taking advantage of the result we acquired from subsubsection 5.1.3, we concluded we need to have a single polarization input in order to eliminate the birefringence. Thus, we can start our COMSOL simulation by defining a linear polarized light always pointing at x direction to simulate our experimental input. Here, it is very important to emphasis the definition of different rotating angles and norms. The COMSOL definition of rotation is shown in Figure 50. The bottom right image shown how elevation angle $\alpha_1$ and azimuth angle $\alpha_2$ are defined in COMSOL, $\vec{a}_1$ and $\vec{a}_2$ represent two square lattice periodic orientations in our simulation. The definitions can be represented by following equations:

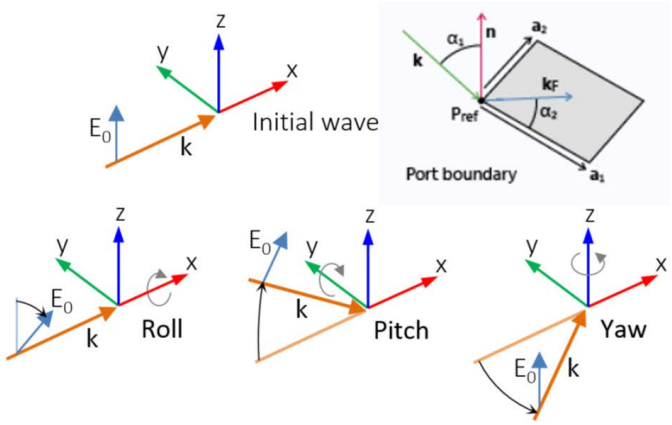


Figure 50: Schematic of the directions for the wave vector k, the electric field $E_0$, and the roll, pitch and yaw rotations from COMSOL software[44]. The top left image represents an initial wave propagating in the x direction with a polarization along the z direction. The top right image shows how parameters are defined.

$$k = k_{parallel} + k_{perpendicular} \tag{66}$$

$$k_{parallel} = k_F = |k| sin\alpha_1 (\vec{a}_1 cos\alpha_2 + n \times \vec{a}_1 sin\alpha_2) \tag{67}$$

Where n is the outward unit normal vector to the boundary, k is the wave vector, $k_{parallel}$ is the projection of k onto the port, $k_{perpendicular}$ is the projection of k to the norm of the port and $k_F$ is the k-vector for Floquet periodicity.

Thus, here we realized an important fact that would cause us a lot of headaches in the future: when neither the azimuth angle nor the elevation angle is 0 or $\pi/2$, the electromagnetic field (or two polarizations) are going to leave the xz and yx plane. We can see this by imagine a rotation shown in Figure 50. The vector nature of the two electric fields here will potentially being unsolvable when we want to use linear Fourier transformations. This issue will be furthur discussed in subsection 7.2.

After the definitions are clear, now we are ready to process the plane wave data we intented to collect by a parametric sweep for both elevation and azimuth angles.

### 7.1.2 COMSOL results

In the COMSOL simulation, the data we used was a scan of 102 × 102 data points for $k_x$ and $k_y$, where k, $k_x$ and $k_y$ are defined as:

$$\begin{aligned} k &= \frac{2\pi}{\lambda} \\ k_x &= \frac{2\pi sin\alpha_1 cos\alpha_2}{\lambda} \\ k_y &= \frac{2\pi sin\alpha_1 sin\alpha_2}{\lambda} \end{aligned} \tag{68}$$

We scanned the $k_x$ and $k_y$ using exponential scan to scan a quarter of the upper semi-sphere of the coordinate system, as presented in Figure 51(a). As shown in the plot, we simulated a region about 30 degrees incident angle, this should be sufficient for our future Gaussian simulation where most of its power remained in 2 degrees. The plot (b) (c) (d) in Figure 51 are all about the bottom right quadrant in plot(a), but all other quadrants are the mirrored images of the one that is plotted. Here from (b) and (c) we are able to determine a very low transmission but high reflection region near 0 incident angle. While for (d) we can see some low "total power" region that might indicate some numerically inaccurate simulation issue, but luckily the region is still far from our center area.

With all the results verified and interpolation method determined, now we are ready to proceed to our next stage of simulation.

## 7.2 Fox and Li simulations

In reality laser resonators are extremely complex multiphysical systems where in practice not all physical quantities are accessible or can be implemented in a efficient and fast resonator model. The scalar Fox and Li algorithm[36][37] to a fully-vectorial light representation has been used in cavity simulations[46][47] that based on the generalization of the scalar Fox-Li algorithm to a fully vectorial field tracing concept. The model discussed in this work gives detailed insight into the shape, polarization state and beam power of the transversal mode of cw, solid-state laser resonators. It should help optical engineers further improve their high quality lasers. For the accurate modeling of these lasers the model includes the following most dominant physical effects:

- Light diffraction, refraction and reflection
- Thermal lensing
- Birefringence
- Light amplification and gain saturation
- Polarization cross-talk and rotation.

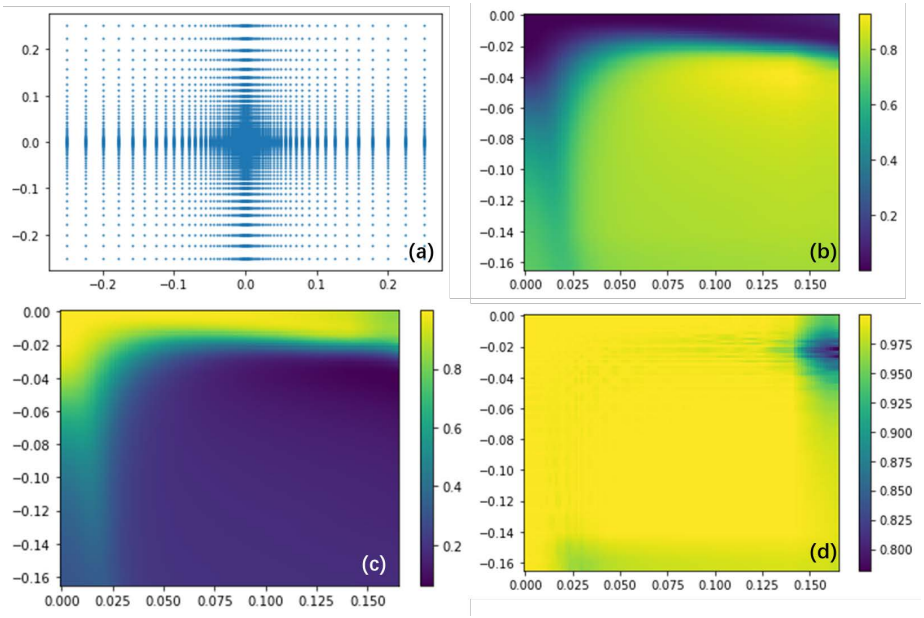


Figure 51: All the axis value here are $k_x/k$ and $k_y/k$. (a)The collections of $k_x$ and $k_y$ data points we collected by COMSOL simulation. (b) The linearly interpolated transmission result for plane waves at different incident angles. (c) The linearly interpolated reflection result for plane waves at different incident angles. (d) The linearly interpolated total power for plane waves at different incident angles. This imply small losses at our operation range.

The limitation of Fox and Li scalar method includes that it can only approximate paraxial optical components and modes only. This limitation could in principle lead to further inaccuracy when the energy distribution in k space components spread to higher angles. We will later find out in our numerical results that this actually happened when our cavity mode has a narrow waist at the photonic crystal membrane side, which corresponds to higher energy component at higher k space angles.

Despite the limitations we discussed about the Fox and Li method, it is still superior compared to other developed method[48][49][50] in its limited numerical burden for the computer when we want to simulate micro-optical components, as we do in our simulation. A full comparison of different known simulation methods can be found at table 2.1 in the phd thesis of Dr.Daniel Christian Asoubar [47].

### 7.2.1 Brief introduction of Fox-Li approach

A scalar Fox-Li algorithm is base on a concept that in the 1960's Fox and Li showed.[37][36] For a laser resonator one or more possible scalar field distributions exist which reproduce themselves after propagating a single time through the complete cavity.

Let us first consider a simple flat mirror Fabry-Perot cavity case with two perfect 100% reflectivity mirrors, where the scalar Fox-Li method is designed for, as shown in Figure 52. Here the Fox-Li method describe that the stable cavity mode can be comprehended as a A scalar, arbitrary paraxial field $E_0(x_0, y_0, z_0)$ given anywhere inside the cavity can be propagated through the resonator, which contains thin optical elements (e.g. a thin aperture that provides some optical losses), by the integral kernel $K^+_{(x,y,x',y')}$, ending up in a full round trip inside the cavity including the two mirrors transformation matrix M1 M2. The inverse propagation can be described similarly by the integral kernel $K^-_{(x,y,x',y')}$. And from the Fox-Li concept, this full round trip inside the cavity should in principle produce an identical field with the only difference which is the attenuation from aperture $\gamma$.

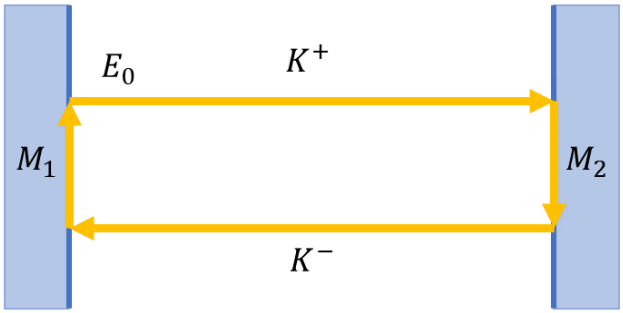


Figure 52: Round trip operator concept for scalar Fox-Li algorithm: A scalar, arbitrary paraxial field $E_0(x_0, y_0, z_0)$ given anywhere inside the cavity can be propagated through the resonator, which contains thin optical elements (e.g. a thin aperture that provides some optical losses), by the integral kernel $K^+_{(x,y,x',y')}$, ending up in a full round trip inside the cavity including the two mirrors transformation matrix M1 M2. The inverse propagation can be described by the integral kernel $K^-_{(x,y,x',y')}$. And from the Fox-Li concept, this full round trip inside the cavity should in principle produce an identical field with the only difference which is the attenuation from aperture $\gamma$.

This algorithm can be expressed as the following equation:

$$\sqrt{\gamma}E_1(x_1, y_1, z_0) = \iint K^+(x_0, y_0, x_1, y_1)M_2K^-(x_0, y_0, x_1, y_1)M_1E_0(x_0, y_0, z_0)dx_0dy_0 \tag{69}$$

This is a general expression for our round trip Fox-Li simulation, where $E_0(x_0, y_0, z_0)$ is the field at an arbitrary starting position $z_0$, and $E_1(x_1, y_1, z_0)$ is the field at the same position after it propagate for a full round trip. The $\gamma$ in front of $E_1(x_1, y_1, z_0)$ is the attenuation of the certain round trip originated from the

aperture we assigned to the cavity. The simulated round trip loss can be described in the following equation:

$$Round\ Trip\ Loss = 1 - \gamma \tag{70}$$

However, for a certain stable cavity mode, we should expect the field $E_1(x_1, y_1, z_0)$ to be identical to $E_0(x_0, y_0, z_0)$ with only a round trip loss constant in front of it. Thus, the expression should becomes Equation 71 for the cavity mode we are searching for.

$$\sqrt{\gamma}E_0(x_0, y_0, z_0) = \iint K^+(x_0, y_0, x_1, y_1)M_2K^-(x_0, y_0, x_1, y_1)M_1E_0(x_0, y_0, z_0)dx_0dy_0 \tag{71}$$

Noted that for our PhC simulation approach, the $\sqrt{\gamma}$ here should also contain a loss originated from our COMSOL simulation and it contained transmission, absorption and higher order losses from PhC membrane simulation.

### 7.2.2 Simulation concepts

After we learned how the Fox-Li algorithm works, the next task is to simulate each optical elements on our optical path to form the algorithm. Here for our simulation method we take M1 as the concave mirror we used with radius of curvature R and M2 as our simulated photonic crystal flat mirror. The light propagated back and forth within our cavity with length L.

For the intracavity propagation of light, we can simulate it by doing a decomposition of real space field into a collection of k space plane-wave components, and the propagation matrix in k space $M_k$ can be discribed as:

$$M_k = e^{-i\pi\lambda(kx^2+ky^2)L} \tag{72}$$

Where $\lambda$ is the wavelength and $L$ is the cavity length.

As for the photonic crystal M2, we have already acquired its k-space transformation matrix from our COMSOL simulation. The last element we should concern about is the concave mirror M1 inside the cavity, the concave mirror can be comprehended as a lens on optical path with focal length equals to $R/2$. Then we are able to simulate the concave mirror in real space, with each points in real space have a gain of phase:

$$M_1 = e^{-i4\pi\frac{R-\sqrt{R^2-x^2-y^2}}{\lambda}} \tag{73}$$

Armed with the round trip simulation procedures, we are now able to logically connect our simulation procedures as shown in Figure 53. Our starting field is demonstrated in real space, and we assume it starts at M1, similar as what we had in experiment(But the sequence here should not matter at all). Then we use the fast Fourier transformation(FFT) module in Python to translate the real space information to k space. After that we will be able to do three k-space transformation in sequence: Propagation L to PhC mirror, PhC mirror transformation M2 and Propagation L back to concave mirror M1. Then the inverse FFT is needed to get our k-field back to real space to be able to use the M1 transformation to simulate the concave mirror. Then we are back to where we starte and set the round trips to n+1, with new starting field $E_{n+1}$ acquired.

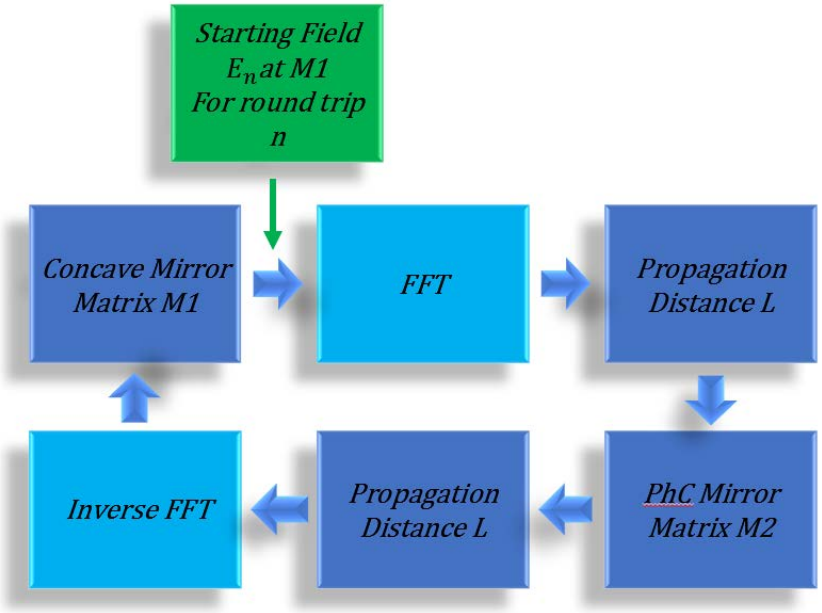


Figure 53: Round trip simulation logic sketch.

We can start our simulation at an arbitrary staring field. Thus, for simplicity reasons, we used a evenly distributed square field to start our simulation. After many round trips(600-1000 round trips in our simulation), we will find the attenuation for each round trips gradually converge to a stable value near 1. This indicate that our simulated cavity mode remains stable for each round trip and this is the simulated optical cavity mode what we wanted to get.

### 7.2.3 Simulation results and analysis

After we finished the Fox and Li simulation in python, now we acquired a stable cavity fundamental mode. With the fundamental mode, we are now able to demonstrate the acquired intracavity mode shape, the transmission data and propagation mode shape in searching of "clover shape" mode.

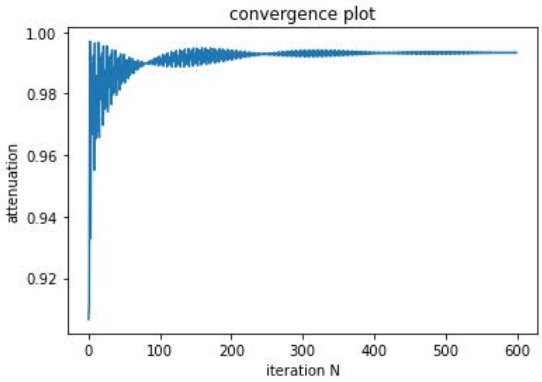


Figure 54: The convergence of attenuation for a evenly distributed square field as starting field of Fox-Li algorithm. We will know the simulation is finished when we see the attenuation eventually converge to a stable value.

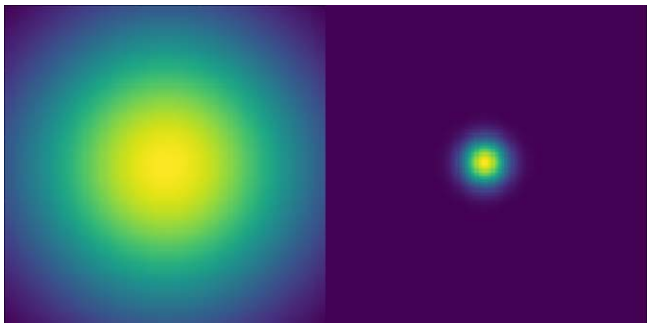

Figure 55: The simulated result for the mode shape inside the cavity. The image on the left is the mode shape near concave mirror and the one on the right is the mode shape image near PhC membrane.

From the intracavity mode, we collected nothing but a gaussian shape mode, as shown in . This simulation results agrees with our earlier observation in Figure 37. In our observation, we acquired the reflection image through the top concave mirror. With the fact that the concave mirror is a coating mirror, the Gaussian reflected light should indicate a Gaussian intracavity mode.

Even though at the near field output as shown in Figure 56 , we observed no clover-shape related phenomenon, the clover shape start to emerge when we include our setup in the simulation. Thus at the 75mm lens beneath the cavity, we can already observe some very clear clover shape beam. This verified what we observed in Figure 43 that around the first mirror we saw a clover shape with huge petals which is quite similar as we what just simulated for the clover shape at 75mm distance to the cavity.

The second part of our verification is about the orientation of our clover beam shape. From our observation in Figure 42 we concluded that the clover shape

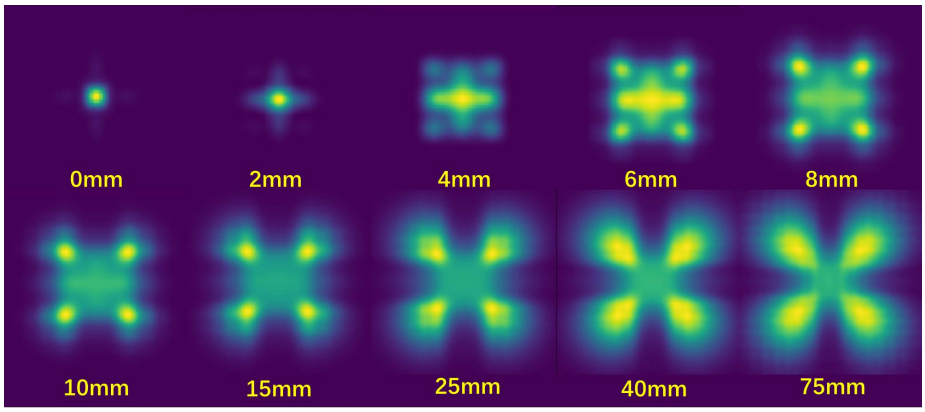


Figure 56: The simulated clover shape image after propagation for different distances. Please note that the images here are scaled differently, since the near field mode shape would be too small otherwise.

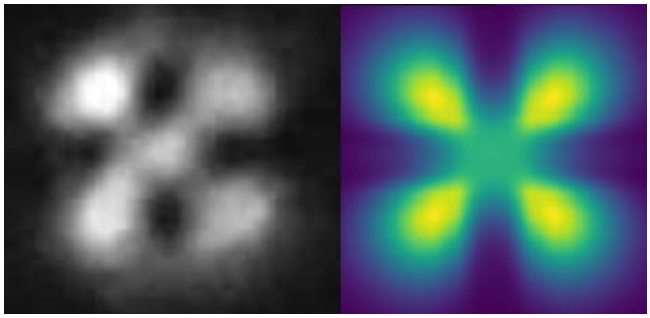

Figure 57: The simulated clover shape image after propagation(right) and the camera captured clover shape after being rotated for 32 degrees(left).

or the lattice orientation was rotated for 32 degrees on our camera, judging from the angles between the green cross and the red cross. Thus, if we align the actual orientation and our simulated directions by rotating the image for 32 degrees, we can get the image in Figure 57. It is quite clear from the image that the orientation from simulation is aligned with what we simulated.

The above simulations and observations was done only under the condition of a $2w_0 = 36\mu m$, we are also curious if the simulation can successfully determine the change of mode shapes at different waists as shown in Figure 45. Thus, we simulated the clover shape at same distance for multiple different beam waists corresponds to the observed beam waists at different cavity lengths as shown in Figure 58. We can see a very interesting blurry effect similar to our former observations, as our simulated beam waist at PhC increased from 36 µm to 72 µm. This is another verification of our theoretical assumptions about the origin of the clover shape.

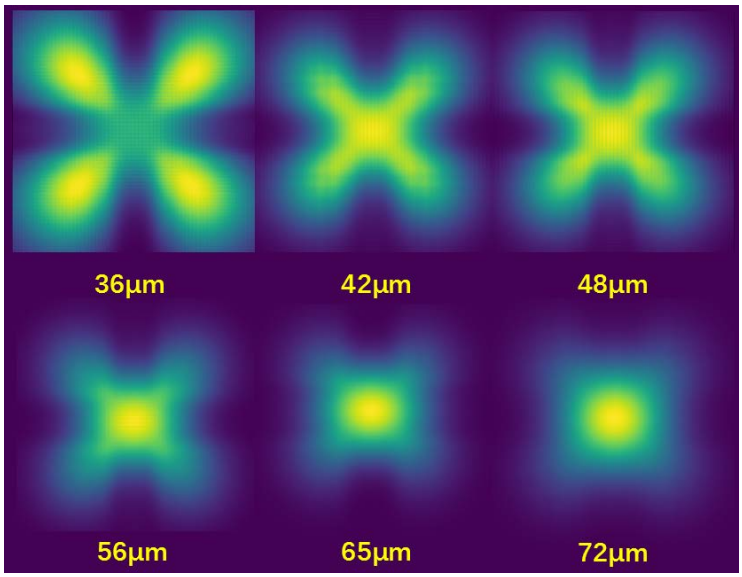


Figure 58: The simulated clover shape image after 75mm propagation for different beam waists. Here the simulated the beam waist was picked based on our former measured waist Figure 45.

The most crucial and final attempt we wanted to challenge our simulation model is to see if it can successfully reproduce any transmission or reflection results from our measurements. We never really raised our expectation to predict any scattering loss we measured, because from subsection 4.5 we realized that it is very possible most of the scattering loss was from imperfections during the fabrication process.

We acquired the total transmission and reflection by determining the sum of all powers of the field before the last penetration of membrane, after being reflected and after being transmitted. The summarized result can be found in Table 6. We can clearly see that something is wrong here, because transmitted power and reflected power add up to bigger than the original power.

From Table 6, even though all the simulation results except the last one are violating the energy conservation law, we can still see that the bigger the waist is, the smaller this violation is. We should notice that the bigger the waist is at the flat mirror(PhC membrane) side, the less energy will be distributed at higher k-space angles. This actually agree with our earlier discussion at subsubsection 7.2.1, that with this scalar approach we used in the simulation, we assumed a paraxial field input. Thus it is not a surprise that we had bad numerical results when we are away from paraxial range.

A more precise description of the flaw of our current situation is that the Fourier transformation we are using regarding all k values as a vector in xy plane, but in reality they cannot be simply processed by linear transformation. Thus the

| **Waist($2w_0$)** | **transmission loss/ppm** | **total loss/ppm** |
|---|---|---|
| 36 | 3211 | 2526 |
| 42 | 1927 | 1308 |
| 48 | 1926 | 1310 |
| 56 | 1467 | 1112 |
| 65 | 1176 | 999 |
| 72 | 1130 | 950 |
| 102 | 983 | 954 |
| 300(imaginary) | 961 | 1027 |

Table 6: The transmission and total loss at different beam waists at membrane. Here the transmission loss is determined by transmittivity, and total loss is determined by reflectivity. Here all the simulation is done neglecting the actual PhC boundary effect(the PhC slab we use has a diameter of 200$\mu$m. Thus the final waist 300$\mu$m is purely imaginary.

solution is that a mapping method is needed to translate all off-plane vectors to the x-y plane, in order for the linear transformation to happen. This can be seen in the earlier explanations of incident angles at subsubsection 7.1.1 and Figure 50. However, since the off-plane vectors cannot be simply mapped to x-y plane while still remaining right angles, this method might have worse errors because we would make two eigen-polarizations cancelling each other.

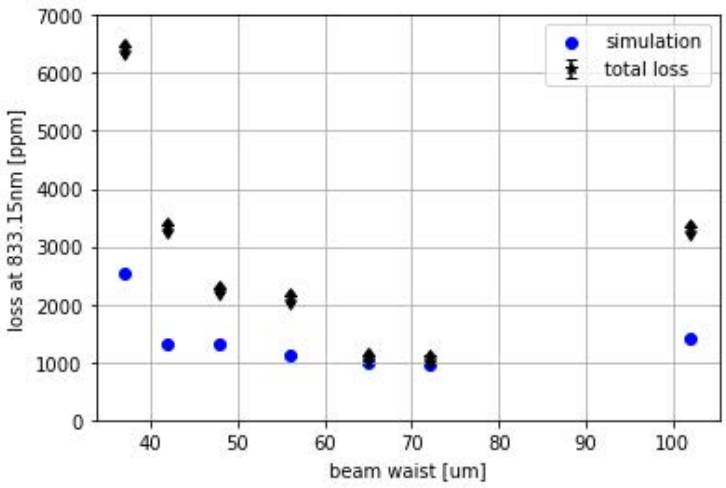


Figure 59: The experimental total loss and the simulated total loss of the membrane. They are both deduced by $1 - reflectivity$.

Even though we are not happy with the transmission simulation results that can barely explain anything for scattering loss, we can still try to provide a comparison of the experimental total loss and simulated total loss for the membrane, as shown in Figure 59.

Here, unsurprisingly, we find that at small waist, the disagreement between simulated results and measured result grows bigger. We can explain the difference by our scalar interpretations of electromagnetic fields. We should also note here that at the beam waist of $102\mu m$, the limited size of PhC defect started to play bigger and bigger role in our experimental results. We can deduce from common Gaussian beam optics [51] that the power distributed outside $r = 100\mu m$ for our $w_0 = 51\mu m$ waist at membrane can be calculated using:

$$\begin{aligned} \frac{P}{P_0} &= e^{-2r^2/w_0^2} \\ &= 458ppm \end{aligned} \tag{74}$$

This value is used in Figure 59 to compensate the loss at $2w_0 = 102\mu m$. However, we should realized that there are two other origins of losses that are not included here. First, the "twisted structures" at the center of the beam that could lead to a significant loss. Second, the boundry effect of photonic crystal. Near the edge of the PhC defect, the period lattice cell number is very limited to the edge, this could lead to a much higher transmission rate. In another word, the effective PhC size $r_{eff}$ should be smaller than the fabricated size $r = 100\mu m$ . This can be the explanation for the differences of simulated and experimental difference at $102\mu$m.

From the results, we are very happy to see a good agreement for the waist near $2w_0 = 70\mu m$. Near this range, we have a waist that is big enough to have limited power in higher angles at k-space, but also small enough to prevent the boundary effect for our photonic crystal. And this is also the waist that we observed the lowest transmission and losses. A beam waist of $2w_0 = 70\mu m$ can be where our membrane should operate at, for any future applications.

In the PhD thesis of Asoubar[47], there is a vertorial simulation method explained about non-resonance cavity simulation. This vertorial method can in principle be used to provide higher numerical accuracy to our simulation. However, due to the limitation of time and the scattering loss of our cavity can never be fully simulated as long as we are still using the current COMSOL simulation results, we decide not to go too far at this direction, especially with the clover beam shape explained.

# 8 Discussions and outlooks

We devote this final chapter to a few remarks on the results of our efforts. We then, retrospectively, discuss how further improvements could have been achieved and discuss suggestions on future explorations.

## 8.1 Result discussions

In this thesis, the main efforts were devoted into the characterizations of the photonic qualities and phenomenons of the PhC membrane fabricated by Dr. Yeghishe Tsaturyan [25]. With the hope of having ultra low scattering loss and highly reflective membranes in the palm of our hand, reality is proved to be against our wish. During the research, we measured how the membrane transmittivity and reflectivity influenced by the wavelength of the laser. The determined a best operational wavelength for the membrane to be about 833nm. We developed and compared 3 different methods to measure the reflectivity and scattering loss of the membrane. Eventually we decided that the "pairing method" prevailed, since it provided us with the most accurate measurement on both scattering loss and transmittivity of the PhC membrane at the target wavelength as well as a insensitivity of coupling rate and losses on optical path that can finish the measurements in a shortest time scale.

During our efforts on finding the best possible cavity parameters to acquire the lowest possible scattering losses, we observed birefriengence, bistability and the clover beam shape out of the cavity. The birefriengence and bistability effects are investigated and eliminated in order for our experiment to continue. The clover beam shape, however, can in principle lead to a bad coupling rate if we were using a multicavity system. After that, some simulation approaches using COMSOL multiphysics and Fox and Li algorithm in Python was done to provide an explanation for the phenomenon.

Eventually, we acquired a PhC membrane results with minimum scattering loss of $780 \pm 10$ppm, and a minimum transmission of $320 \pm 10$ppm. Results on several other membranes with much higher scattering loss are also presented to complete the tests. For the completeness of the measurements, we did the measurements for different cavity lengths, different wavelengths and different x/y axis position on the membrane. These results can of use to determine the best operation range for all the similar photonic crystal membranes.

## 8.2 Outlooks

Sadly, the result so far is insufficient for the membrane-at-the-back or the membrane-outside-cavity approaches to work effectively. However, the process of how those results were achieved and the explanations for the clover-beam shape phenomenon can be an essential step for future research involving photonic crystal membranes.

A new generation of PhC membranes has been made by Anders Simonsen and his colleagues, with up-to-date fabrication methods. Thus, in the next step of our experiment, we can first characterize the photonic qualities of these new wafers and hope for some better results.

Apart from testing the new membranes, an investigation of the origins of the 800ppm scattering loss should be accomplished for the next research step. We made some early assumptions about the holes not being cylinder as we assumed but instead having a bigger radius for the top circle. This was the result of the imperfect fabrication and could be the origin of this quite universal scattering loss. The aftermath of this effect can be verified by doing a COMSOL simulation with a smaller bottom radius cylinder.

Another important test we did not have enough time to accomplish is the measurement of how the low-temperature influences the photonic reflectivities and other photonic characteristics. As we learn from solid physics, the size of photonic holes will change at different temperatures. This could result in a decrease in peak reflectivity frequency at a lower temperature(4K for helium). This phenomenon is quite important and needs to be investigated sooner or later.

## 8.3 Acknowledgments

It has been a special year for me, for the lab, and for the world. The long-lasting Covid-19, the war, and the international stress influenced and depressed everyone more or less. But I am very lucky to be warmly welcomed in the best lab I have ever been along with the best people in quantum physics.

First, I would like to thank Professor Eugene Polzik for welcoming me to one of the best research groups in the world. He provided me with an amazing thesis topic which helped me develop my creativity in experimental physics and self-motivated working ability.

Secondly, I want to show my gratitude to Anders Simonsen, who helped me as an expert on simulation as well as general physics topics whenever I asked. Your detailed introduction was precious to me as a newbie to the COMSOL simulation, and I will remember our long discussions on various physics topics. And I also want to thank Ivan, Beñat, Østfeldt, Rebecca, Christian, Peyman, Jonas, and Jun Jia for their help and ideas on my experiment when I was stuck and helpless in the lab. The brilliant ideas and experiences I gained from Jörg and JB.

Most importantly, I need to thank Georg Enzian for transferring me his knowledge about the cavity optomechanics as well as all the guidance on coding and simulation. But Georg helped me way more than physical knowledge. You always showed up in time during the time when I was stressed because of the project and my personal life. It has been hard for me during recent months as

a Chinese because of all the travel restrictions, and I haven't seen my family for a year. That is why I really needed and appreciated our talk and exchange about life and purpose. You are the definition of a true mentor and a very good friend to me. Thank you for everything!

Finally, I have been staying in Denmark for two years without any chance to see my family and loved ones in my home country. I want to thank my family, especially my parents, for all the selfless support and trust during the difficult time, and I feel sorry for not being able to express my love to you in person. And to Yueran Meng, who loved me and supported me wholeheartedly during my study, I hope I can do the same for you and pay back your love in the future. Special thanks to Nong Sun, you offered me all you love during my thesis writing as if a bright lantern guided my soul out of the swamp of reality. I hope our paths in life will finally intertwine in the future. I would never make it without the love and supports from all of you.

I am grateful for what life has brought me over the last two years, and I wish the best future for everyone here at Niels Bohr Institute. Thank you all very much for the life we shared together!

# References


[1] David S Bradshaw and David L Andrews. Manipulating particles with light: radiation and gradient forces. *European Journal of Physics*, 38(3):034008, 2017.

[2] Yeghishe Tsaturyan, Andreas Barg, Eugene S Polzik, and Albert Schliesser. Ultracoherent nanomechanical resonators via soft clamping and dissipation dilution. *Nature nanotechnology*, 12(8):776–783, 2017.

[3] Georg Enzian, Magdalena Szczykulska, Jonathan Silver, Leonardo Del Bino, Shuangyou Zhang, Ian A Walmsley, Pascal Del'Haye, and Michael R Vanner. Observation of brillouin optomechanical strong coupling with an 11 ghz mechanical mode. *Optica*, 6(1):7–14, 2019.

[4] AM Jayich, JC Sankey, BM Zwickl, C Yang, JD Thompson, SM Girvin, AA Clerk, F Marquardt, and JGE Harris. Dispersive optomechanics: a membrane inside a cavity. *New Journal of Physics*, 10(9):095008, 2008.

[5] Massimiliano Rossi, David Mason, Junxin Chen, Yeghishe Tsaturyan, and Albert Schliesser. Measurement-based quantum control of mechanical motion. *Nature*, 563(7729):53–58, 2018.

[6] David Mason, Junxin Chen, Massimiliano Rossi, Yeghishe Tsaturyan, and Albert Schliesser. Continuous force and displacement measurement below the standard quantum limit. *Nature Physics*, 15(8):745–749, 2019.

[7] Junxin Chen, Massimiliano Rossi, David Mason, and Albert Schliesser. Entanglement of propagating optical modes via a mechanical interface. *Nature communications*, 11(1):1–6, 2020.

[8] Xu Chen, Clément Chardin, Kevin Makles, Charles Caër, Sheon Chua, Rémy Braive, Isabelle Robert-Philip, Tristan Briant, Pierre-François Cohadon, Antoine Heidmann, et al. High-finesse fabry–perot cavities with bidimensional si3n4 photonic-crystal slabs. *Light: Science & Applications*, 6(1):e16190–e16190, 2017.

[9] Thorlab concave mirror data page. https://www.thorlabs.com/newgrouppage9.cfm?objectgroup_id=14093. Accessed: 2022-03-30.

[10] Peter W Milonni and Joseph H Eberly. *Laser physics*. John Wiley & Sons, 2010.

[11] Refractive index of si3n4, silicon nitride, sin, sion. https://www.filmetrics.com/refractive-index-database/Si3N4. Accessed: 2022-03-30.

[12] Jack C Sankey, Cheng Yang, Benjamin M Zwickl, Andrew M Jayich, and Jack GE Harris. Strong and tunable nonlinear optomechanical coupling in a low-loss system. *Nature Physics*, 6(9):707–712, 2010.

[13] Herwig Kogelnik. On the propagation of gaussian beams of light through lenslike media including those with a loss or gain variation. *Applied Optics*, 4(12):1562–1569, 1965.

[14] H. Kogelnik and T. Li. Laser beams and resonators. *Appl. Opt.*, 5(10):1550–1567, Oct 1966.

[15] JD Thompson, BM Zwickl, AM Jayich, Florian Marquardt, SM Girvin, and JGE Harris. Strong dispersive coupling of a high-finesse cavity to a micromechanical membrane. *Nature*, 452(7183):72–75, 2008.

[16] Florian Elste, SM Girvin, and AA Clerk. Quantum noise interference and backaction cooling in cavity nanomechanics. *Physical review letters*, 102(20):207209, 2009.

[17] I Mahboob, N Perrissin, K Nishiguchi, D Hatanaka, Y Okazaki, A Fujiwara, and H Yamaguchi. Dispersive and dissipative coupling in a micromechanical resonator embedded with a nanomechanical resonator. *Nano letters*, 15(4):2312–2317, 2015.

[18] Alexandr Karpenko and Sergey P Vyatchanin. Dissipative coupling, dispersive coupling, and their combination in cavityless optomechanical systems. *Physical Review A*, 102(2):023513, 2020.

[19] AK Tagantsev, IV Sokolov, and ES Polzik. Dissipative versus dispersive coupling in quantum optomechanics: Squeezing ability and stability. *Physical Review A*, 97(6):063820, 2018.

[20] Alexander K Tagantsev and Eugene S Polzik. Dissipative optomechanical coupling with a membrane outside of an optical cavity. *Physical Review A*, 103(6):063503, 2021.

[21] Mingyun Yuan, Vibhor Singh, Yaroslav M Blanter, and Gary A Steele. Large cooperativity and microkelvin cooling with a three-dimensional optomechanical cavity. *Nature communications*, 6(1):1–6, 2015.

[22] Markus Aspelmeyer, Tobias J Kippenberg, and Florian Marquardt. Cavity optomechanics. *Reviews of Modern Physics*, 86(4):1391, 2014.

[23] Kjetil Børkje. Critical quantum fluctuations and photon antibunching in optomechanical systems with large single-photon cooperativity. *Physical Review A*, 101(5):053833, 2020.

[24] Vincent Dumont, Simon Bernard, Christoph Reinhardt, Alex Kato, Maximilian Ruf, and Jack C Sankey. Flexure-tuned membrane-at-the-edge optomechanical system. *Optics express*, 27(18):25731–25748, 2019.

[25] Yeghishe Tsaturyan. *Ultracoherent soft-clamped mechanical resonators for quantum cavity optomechanics*. PhD thesis, University of Copenhagen, Faculty of Science, Niels Bohr Institute, Danish ..., 2019.

[26] William Hvidtfelt Padkær Nielsen. *Quantum cavity optomechanics with phononic bandgap shielded silicon nitride membranes*. PhD thesis, University of Copenhagen, Faculty of Science [Niels Bohr Institute], 2016.

[27] Martin Suter and Peter Dietiker. Calculation of the finesse of an ideal fabry–perot resonator. *Applied optics*, 53(30):7004–7010, 2014.

[28] Ivanp Kaminow. Polarization in optical fibers. *IEEE Journal of Quantum Electronics*, 17(1):15–22, 1981.

[29] F Genereux, SW Leonard, HM Van Driel, A Birner, and U Gösele. Large birefringence in two-dimensional silicon photonic crystals. *Physical Review B*, 63(16):161101, 2001.

[30] Soan Kim, Chul-Sik Kee, and Chung Ghiu Lee. Modified rectangular lattice photonic crystal fibers with high birefringence and negative dispersion. *Optics Express*, 17(10):7952–7957, 2009.

[31] A Dorsel, John D McCullen, Pierre Meystre, E Vignes, and H Walther. Optical bistability and mirror confinement induced by radiation pressure. *Physical Review Letters*, 51(17):1550, 1983.

[32] Pierre Meystre, Ewan M Wright, JD McCullen, and E Vignes. Theory of radiation-pressure-driven interferometers. *JOSA B*, 2(11):1830–1840, 1985.

[33] João P Moura, Richard A Norte, Jingkun Guo, Clemens Schäfermeier, and Simon Gröblacher. Centimeter-scale suspended photonic crystal mirrors. *Optics express*, 26(2):1895–1909, 2018.

[34] Christina J Hood, HJ Kimble, and Jun Ye. Characterization of high-finesse mirrors: Loss, phase shifts, and mode structure in an optical cavity. *Physical Review A*, 64(3):033804, 2001.

[35] Ebrahim Karimi, Sebastian A Schulz, Israel De Leon, Hammam Qassim, Jeremy Upham, and Robert W Boyd. Generating optical orbital angular momentum at visible wavelengths using a plasmonic metasurface. *Light: Science & Applications*, 3(5):e167–e167, 2014.

[36] Arthur G Fox and Tingye Li. Resonant modes in a maser interferometer. *Bell System Technical Journal*, 40(2):453–488, 1961.

[37] AG Fox and Tingye Li. Modes in a maser interferometer with curved and tilted mirrors. *Proceedings of the IEEE*, 51(1):80–89, 1963.

[38] SA Degtyarev, VV Podlipnov, Payal Verma, and SN Khonina. 3d simulation of silicon micro-ring resonator with comsol. In *International Conference on Micro-and Nano-Electronics 2016*, volume 10224, page 102241L. International Society for Optics and Photonics, 2016.

[39] DF Santos, Ariel Guerreiro, and José Manuel Baptista. Numerical investigation of a refractive index spr d-type optical fiber sensor using comsol multiphysics. *Photonic sensors*, 3(1):61–66, 2013.

[40] Javier Alda. Laser and gaussian beam propagation and transformation. *Encyclopedia of optical engineering*, 999, 2003.

[41] Yuanyuan Wang, Deyuan Chen, Gang Zhang, Juebin Wang, and Shangbin Tao. A super narrow band filter based on silicon 2d photonic crystal resonator and reflectors. *Optics communications*, 363:13–20, 2016.

[42] Yan Pennec, Jérôme O Vasseur, Bahram Djafari-Rouhani, Leonard Dobrzyński, and Pierre A Deymier. Two-dimensional phononic crystals: Examples and applications. *Surface Science Reports*, 65(8):229–291, 2010.

[43] Toke Vibel. photonic crystal and high-contrast gratings for high finesse optomechanics, 2018.

[44] Walter Frei. How to model the optical properties of rough surfaces, 2017.

[45] Herbert R Philipp. Optical properties of silicon nitride. *Journal of the Electrochemical Society*, 120(2):295, 1973.

[46] Daniel Asoubar and Frank Wyrowski. Fully vectorial laser resonator modeling of continuous-wave solid-state lasers including rate equations, thermal lensing and stress-induced birefringence. *Optics express*, 23(15):18802–18822, 2015.

[47] Daniel Asoubar et al. *Simulation of continuous-wave solid-state laser resonators using field tracing and a fully vectorial Fox-Li algorithm.* PhD thesis, 2016.

[48] Yong-Zhen Huang, Wei-Hua Guo, and Qi-Ming Wang. Analysis and numerical simulation of eigenmode characteristics for semiconductor lasers with an equilateral triangle micro-resonator. *IEEE journal of quantum electronics*, 37(1):100–107, 2001.

[49] Konrad Altmann, Christoph Pflaum, and David Seider. Modeling and computation of laser cavity eigenmodes. In *Solid State Lasers and Amplifiers*, volume 5460, pages 204–211. SPIE, 2004.

[50] Péter Nyakas. Full-vectorial three-dimensional finite element optical simulation of vertical-cavity surface-emitting lasers. *Journal of lightwave technology*, 25(9):2427–2434, 2007.

[51] Masud Mansuripur. Gaussian beam optics. *Opt. Photonics News*, 12(1):44–47, 2001.